6

CHAPTER 6: NUMERICAL OPTIMISATION OF CONJUGATE HEAT TRANSFER IN COOLING CHANNELS WITH DIFFERENT CROSS-SECTIONAL SHAPES[3],[4]

6.1. INTRODUCTION

This chapter focuses on the study of the numerical approximation of three-dimensional conjugate heat transfer in heat generated solid structures. It examines the geometric optimisation of a fixed and finite global volume of solid materials in an array of cooling channels with different cross-sectional configurations which experience a uniform internal heat generation, which will result in the minimal global thermal resistance. The objective is the building of a smaller construct to form a larger construct body that will minimise the global thermal resistance or, inversely, maximise the heat transfer rate density (the total heat transfer rate per unit volume).

[3] This research chapter, together with chapter 5 has been published in part: O.T. Olakoyejo, T. Bello-Ochende and J.P Meyer, "Constructal conjugate cooling channels with internal heat generation", *International Journal of Heat and Mass Transfer*. Vol. 55, pp. 4385 - 4396, 2012.

[4] This research chapter, together with chapter 5 has been published in part: J.P Meyer; O.T. Olakoyejo and T. Bello-Ochende, "Constructal optimisation of conjugate triangular cooling channels with internal heat generation", *International communication of Heat and Mass Transfer*, Vol. 39, pp. 1093 - 1100, 2012.

This is achieved by forcing a coolant to the heated spot in a fast and efficient way so as to drastically reduce the peak temperature at any point inside the volume that needs cooling. The optimisation process is carried out numerically under total fixed-volume and manufacturing constraints. As in all problems of constructal design, the configuration (shape, size) is unknown and must be determined. The mathematical optimisation algorithm described in Chapter 4 is introduced to search and identify the design variables at which the system will perform at an optimum. Thus the minimum thermal resistance between the fixed volume and the cooling fluid is obtained as the desired objective function for all the cases of geometrical shape studied. The present numerical results and the analytical solutions proposed in Chapter 5 are compared for each case study. The numerical solutions of all the case studies are also compared before the chapter is concluded.

6.2. CASE STUDY 1: CYLINDRICAL AND SQUARE COOLING CHANNEL EMBEDDED IN HIGH-CONDUCTING SOLID

This case study builds on the research previously carried out by Ordonez [117]. He conducted a two-dimensional heat transfer analysis in a heat-generated volume with an array of cylindrical cooling channels and air as the working fluid in which he minimised the global thermal resistance.

The present case study examines the three-dimensional numerical thermal resistance analysis in a heat-generated volume with separate cylindrical and square cooling channels and water as cooling fluid. A computational elemental volume cell will be modelled by using the symmetrical property of heat distribution. However, a mathematical optimisation algorithm (DYNAMIC-Q) will be used to find the optimal peak temperature hence (thermal resistance) by varying the geometric parameters of the geometries subject to various constraints. The various heat transfer and optimisation results obtained will then be compared with analytical solutions of Chapter 5 and those found in the literature.

6.2.1. Computational model

The physical circular and square configurations are shown schematically in Figure 5.1(a) and 5.1(b). The system consists of parallel cooling channels of length L and fixed global volume, V . The internal heat generation in the solid material is q_s''' . An elemental volume, v_{el} , consisting of a cooling channel and the surrounding solid, was used for analysis because it was assumed that heat distribution inside the structure was symmetrical. However, the elemental volume v_{el} is not fixed and is allowed to morph by varying the cross-sectional shape v_c of the cooling channel for fixed porosity. The heat transfer in the elemental volume is a conjugate problem, and it combines heat conduction in the solid and the convection in the working fluid. These

two modes of heat transfer are coupled together through the continuity of heat flux at the solid-fluid interface.

6.2.1.1. Design variables

In Figure 6.1, an elemental volume, v_{el}, constraint is considered to be composed of an elemental cooling channel of hydraulic diameter, d_h, and the surrounding solid of thickness s (spacing between channels). These variables are defined as follows:

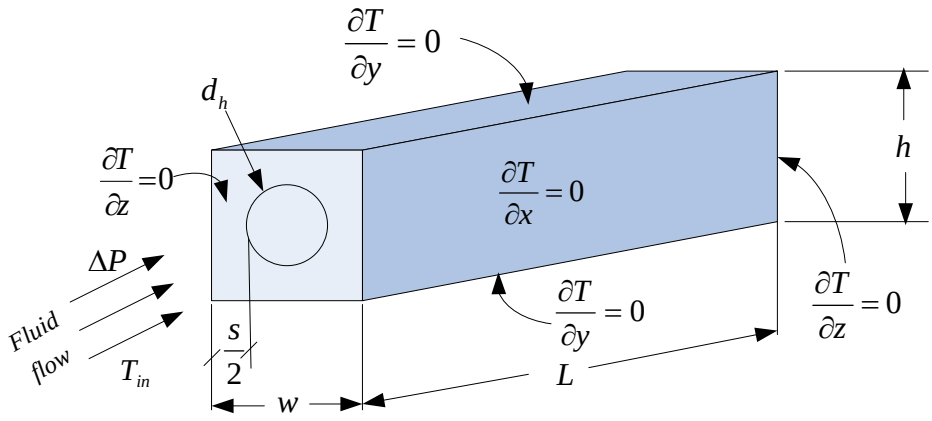

(a)

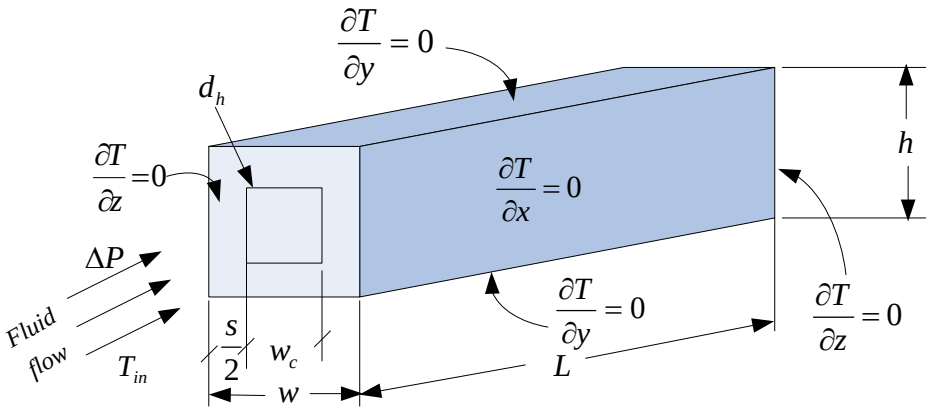

(b)

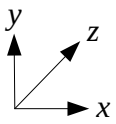

Figure 6. 1 : The boundary conditions of the three-dimensional computational domain of the cooling channel: (a) cylinder (b) square

$$w = h \tag{6.1}$$

$$v_{el} = w^2 L \tag{6.2}$$

$$w = d_h + s \tag{6.3}$$

Therefore, the total number of channels in the structure arrangement can be defined as

$$N = \frac{HW}{\left(d_h + s\right)^2} \tag{6.4}$$

However, the void fraction or porosity of the unit structure can be defined [117] as:

$$\phi = \frac{v_c}{v_{el}} \approx \left(\frac{d_h}{w}\right)^2 \tag{6.5}$$

The fundamental problem under consideration is the numerical optimisation of the hydraulic diameter, d_h, and spacing between channels, s, which corresponds to the minimum resistance of a fixed volume for a given pressure difference. The optimisation is evaluated from the analysis of the extreme limits of $\left(0 \le v_{el} \le \infty\right)$, $\left(0 \le d_h \le \infty\right)$ and the extreme limits of $\left(0 \le s \le \infty\right)$. The optimal values of the design variables within the prescribed interval of the extreme limits exhibit the minimum thermal resistance.

The temperature distribution in the model was determined by solving numerically for the conservation of mass, momentum and energy equations (Equations (3.31) to (3.38) of Chapter 3). The discretised three-dimensional computational domains of the circular and square configurations are shown in Figure 6.2. The cooling fluid was water, which is assumed to be in single-phase, steady, and a Newtonian fluid with constant thermo-physical properties. The water was forced through the cooling channels by a specified pressure difference, ΔP, across the axial length of the structure. Other assumptions imposed on the two configurations model are as follows:

The continuity of the heat flux at the interface between the solid and the liquid is given as:

$$k_s \frac{\partial T}{\partial n}\bigg| = k_f \frac{\partial T}{\partial n}\bigg| \tag{6.6}$$

A no-slip boundary condition is specified at the wall of the channel,

$$\vec{u} = 0 \tag{6.7}$$

and at the inlet ($x = 0$)

$$u_x = u_y = 0 \tag{6.8}$$

$$T = T_{in} \tag{6.9}$$

$$P = \frac{Be\alpha\mu}{L^2} + P_{out} \tag{6.10}$$

where, Be is the dimensionless pressure difference called the Bejan number [182, 183].

At the channel outlet $(x = L)$, a zero normal stress is prescribed, and

$$P_{out} = 1\ atm \tag{6.11}$$

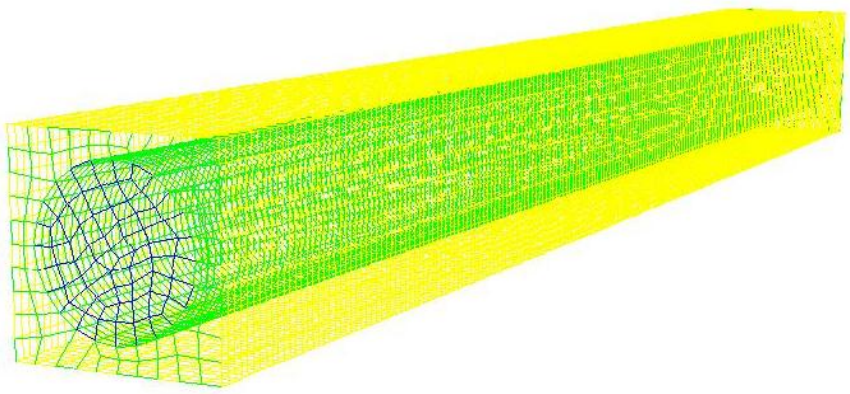

(a)

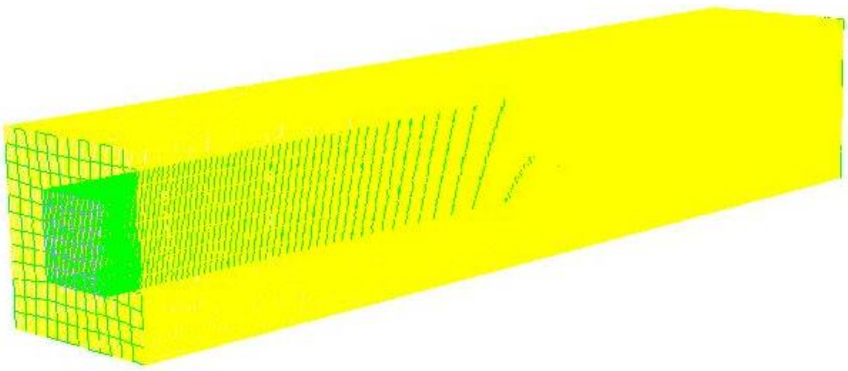

(b)

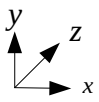

Figure 6. 2 : The discretised 3-D computational domain: (a) cylinder (b) square

At the solid boundaries, all the outside walls and plane of symmetry of the solid structure were modelled as adiabatic as shown in Figure 6.1. Hence

$$\nabla T = 0 \tag{6.12}$$

and an internal heat generation, q_s''' is assumed in the solid material.

The measure of performance is the minimum global thermal resistance, which could be expressed in a dimensionless form as:

$$R_{\min} = \frac{k_f \left(T_{\max} - T_{in}\right)_{\min}}{q_s''' L^2} \tag{6.13}$$

and it is a function of the optimised design variables and the peak temperature,

$$R_{\min} = f\left(d_{h_{opt}},\ s_{opt},\ v_{el_{opt}},\ T_{\max_{\min}}\right) \tag{6.14}$$

where R_{min} is the minimised dimensionless thermal resistance for the optimised design variables. The inverse of R_{min} is the maximised overall global thermal conductance.

6.2.2. Numerical procedure

The simulation procedure began by fixing the length of the channel, applied pressure difference, porosity, internal heat generation and material properties. We also kept varying the values of elemental volume and the hydraulic diameter of the channel in order to identify the best (optimal) internal and external geometries that minimised the peak temperature.

The numerical solution of continuity, momentum and energy equations (Equations (3.1) to (3.8) of Chapter 3) along with the boundary conditions (Equations (6.6) to (6.12)) was obtained by using a three-dimensional commercial package FLUENT™ [199], which employs a finite volume method. The details of the method are explained by Patankar [203]. The computational fluid dynamics package was coupled with the geometry and mesh generation package GAMBIT [201] using MATLAB [219] to allow the automation and running of the simulation process. After the simulation converged, an output file was obtained containing all the necessary simulation data and results for the post-processing and analysis. The computational

domain was discretised using hexahedral/wedge elements. A second-order upwind scheme was used to discretise the combined convection and diffusion terms in the momentum and energy equations. The SIMPLE algorithm was then employed to solve the coupled pressure-velocity fields of the transport equations. The solution is assumed to be converged when the normalised residuals of the mass and momentum equations fall below 10^{-6} and while the residual convergence of energy equation was set to less than 10^{-10}. The number of grid cells used for the simulations varied for different elemental volume and porosities. However, grid independence tests for several mesh refinements were carried out to ensure the accuracy of the numerical results. The convergence criterion for the overall thermal resistance as the quantity monitored is

$$\gamma = \frac{\left|\left(T_{\max}\right)_i - \left(T_{\max}\right)_{i-1}\right|}{\left|\left(T_{\max}\right)_i\right|} \leq 0.01 \tag{6.15}$$

where i is the mesh iteration index. The mesh becomes more refined as i increases. The $i-1$ mesh is selected as a converged mesh when the criterion Equation (6.15) is satisfied. The model and solution were implemented using an Intel Core(TM) 2Duo 1.6 GHz PC with 2 GB of DDRam. The average time of the simulation and convergence for each operating value of design variable and dimensionless pressure difference number was in the range of 1– 4 hours.

6.2.3. Grid analysis and code validation

To ensure accurate results, several grid independence test were conducted until a mesh size with negligible changes in peak temperature was obtained. Figures 6.3 and 6.4 show the grid independence test for cylindrical and square configurations respectively, for $v_{el} = 0.4\,\text{mm}^3$ and $\phi = 0.2$ and $\Delta P = 50\ kPa$.

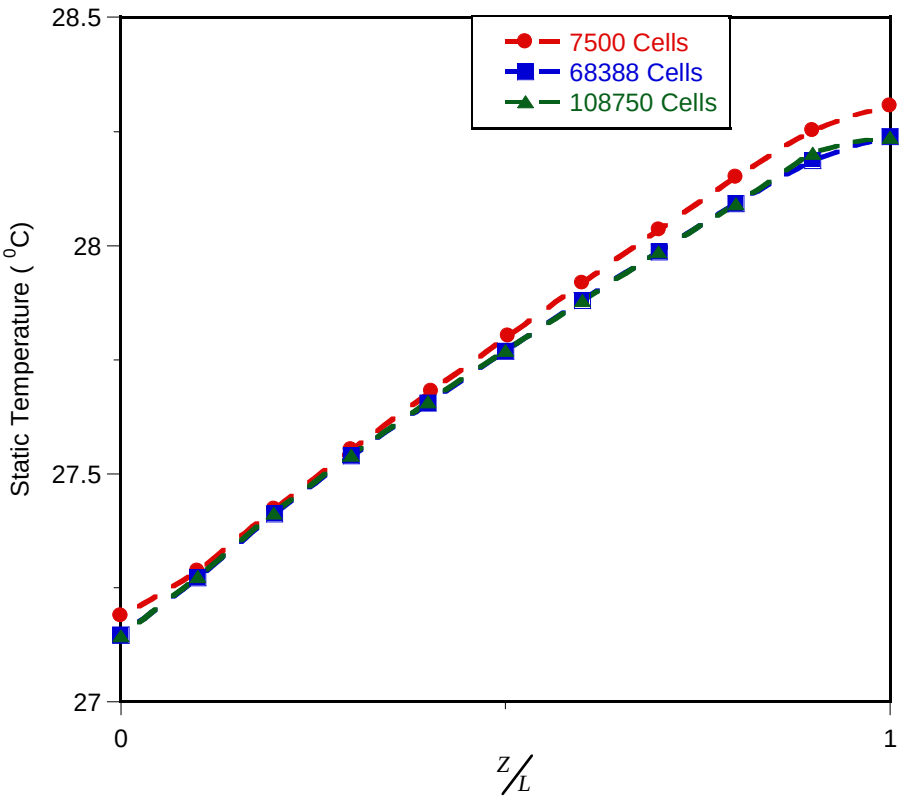

Figure 6. 3: Grid independent test for cylindrical configuration at fixed pressure difference and porosity

Computational cell densities of 7 500, 68 388 and 108 750 were used for the cylindrical configuration grid independence test. It was observed that almost identical results were predicted when 68 388 and 108 750 cells were used. Therefore, a further

increase in the cell density beyond 68 388 has a negligible effect on the numerical result. Again, computational cell densities of 16317, 26 688 and 50 000 were used for the square configuration grid independence test. It was observed that almost identical results were predicted when 26 688 and 50 000 cells were used. Therefore, any further increase in the cell density beyond 26 688 has a negligible effect on the numerical result.

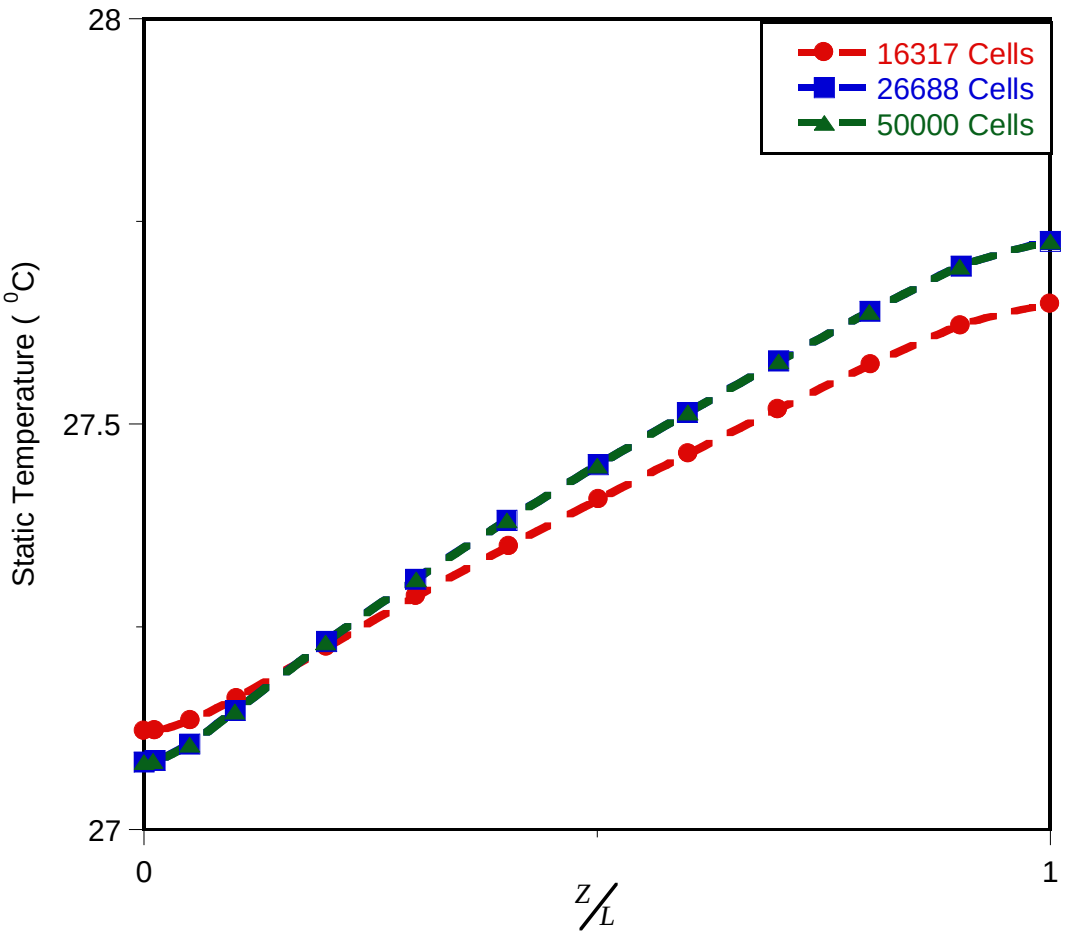

Figure 6. 4 : Grid independence test for a square configuration at fixed pressure difference and porosity

The validation of the numerical simulation was also carried out by comparing the present simulation for a circular configuration with the dimensionless temperature simulation of Ordonez [117] as shown in Figure 6.5. The curves were found to be similar in trend, while the optimised hydraulic diameters were also found to be in good agreement. However, the difference in the dimensionless maximum thermal temperature may be due to the kind of mesh refinement used. Our computation mesh is more refined than that of Ordonez [117].

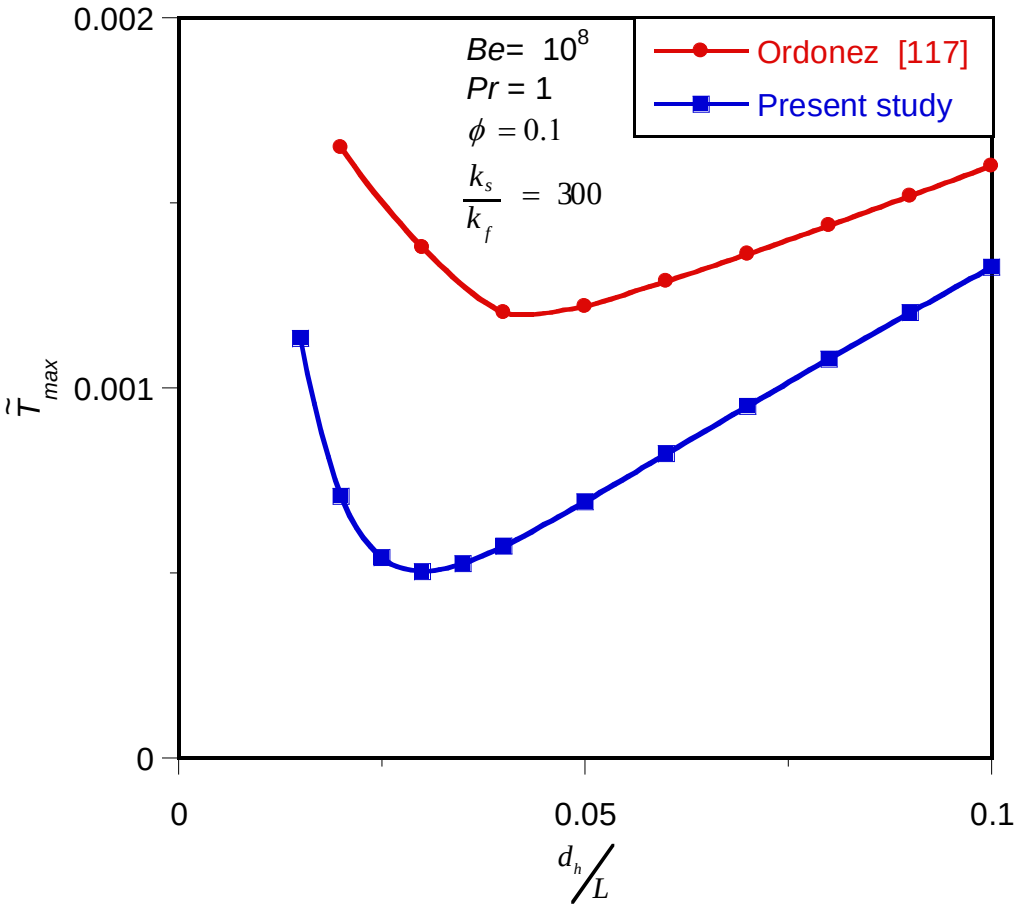

Figure 6. 5 : Thermal resistance curves: present study and that of Ordonez [117]

6.2.4. Numerical results using a traditional method

In this section, the numerical results are presented using a traditional method by post-processing the simulation data and results manually. We present the results for the case when the elemental volume of the structure was in the range of $0.025\ \text{mm}^3 \leq v_{el} \leq 5\ \text{mm}^3$; the porosities ranged between $0.1 \leq \phi \leq 0.2$; the fixed length of L was 10 mm and fixed applied pressure differences of $\Delta P = 50$ kPa. The thermal conductivity of the solid structure (silicon) was 148 W/m.K; and the internal heat generation within the solid was taken to be fixed at 100 kW/m^3. The thermo-physical properties of water [202] used in this study were based on water at 300 K and the inlet water temperature was therefore fixed at this temperature.

Figures 6.6 and 6.7 show the existence of an optimal hydraulic diameter and channel spacing in which the peak temperature is minimised at any point in the channel for the two configurations studied.

Figure 6.6 shows the peak temperature as a function of the hydraulic diameter of the channels. It shows that there exists an optimal channel hydraulic diameter, which lies in the range $0.005 \leq d_h/L \leq 0.022$ and minimises the peak temperature. The minimum peak temperature exist is in achieved when the optimal channel spacing exists in the range of $0.005 \leq s/L \leq 0.035$. These indicate that the peak temperature decreases as

global design variables increase and that maximal (optimal) values of the design variables are reached beyond which the peak temperature begins to increase.

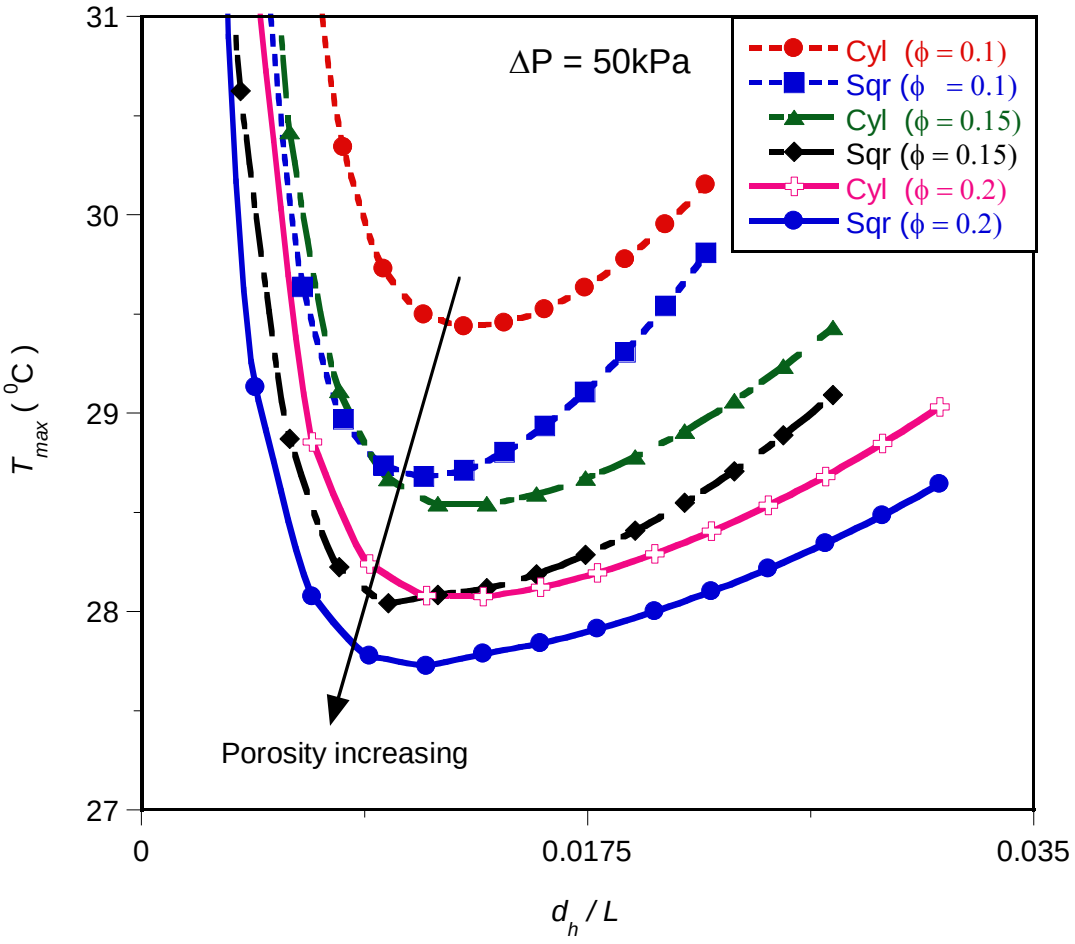

Figure 6. 6 : Effect of optimised hydraulic diameter d_h on the peak temperature

Thus, the global peak temperature decreases as the design variables decrease – until it gets to the optimal design values. Any increase or decrease in the design variable beyond the optimal values indicates that the working fluid is not properly engaged in the cooling process, which is detrimental to the global performance of the system.

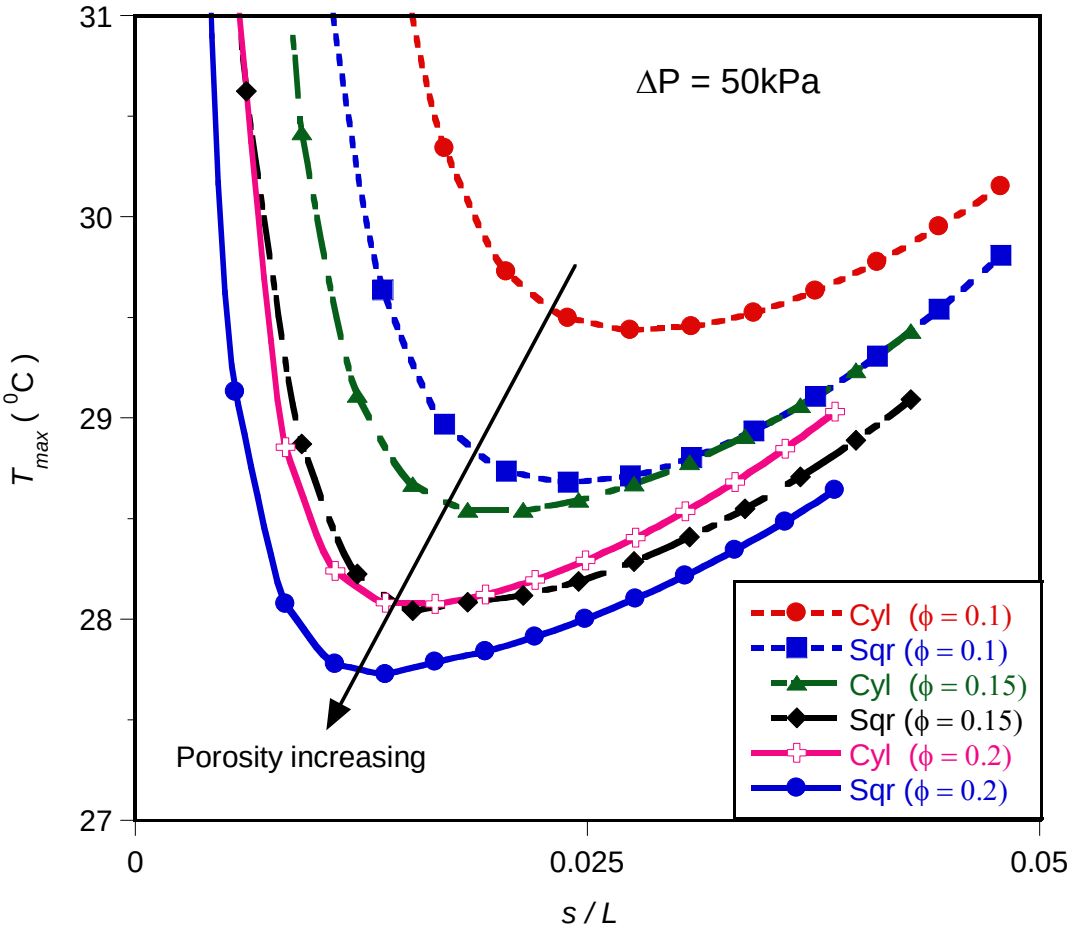

Figure 6. 7: Effect of optimised channel spacing on the peak temperature

Also, the elemental volume of the structure has a strong effect on the peak temperature as shown in Figure 6.8. It shows that there is an optimal elemental volume of the structure that minimises the peak temperature and this lies in the range of $0.2\ \text{mm}^3 \leq v_{el} \leq 2\ \text{mm}^3$.

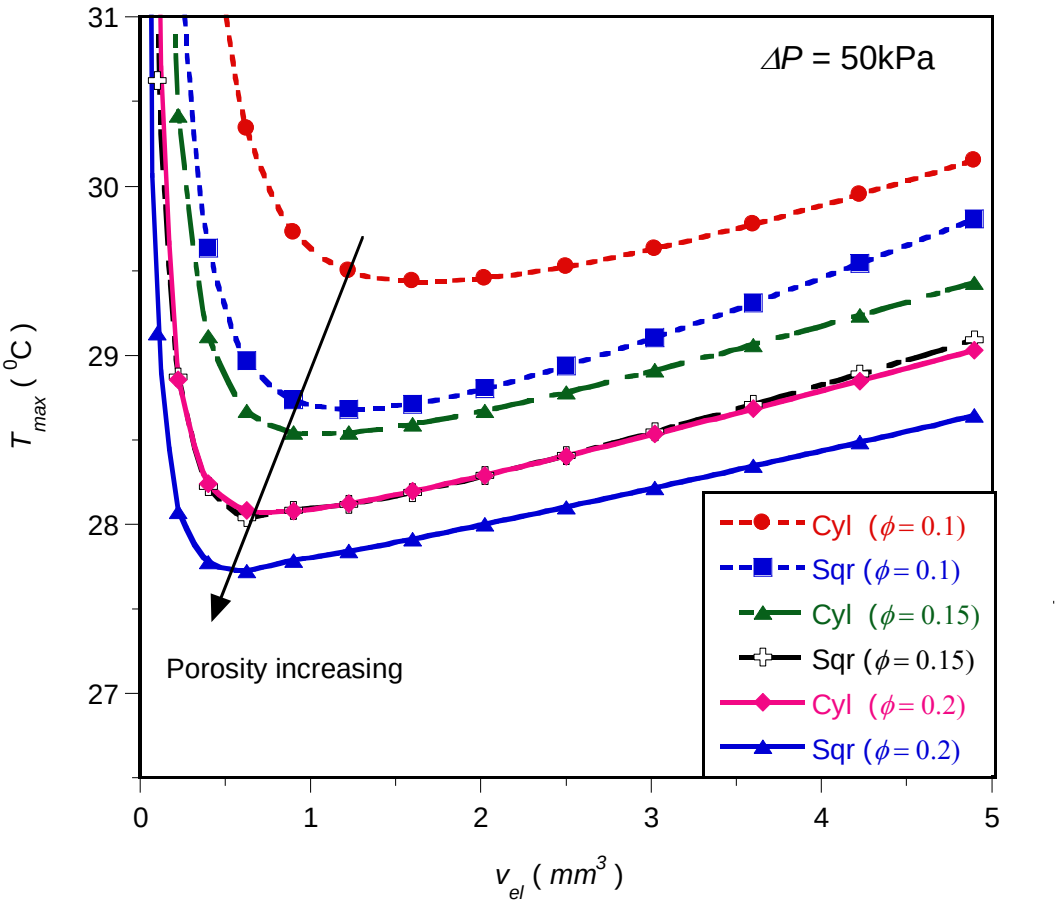

Figure 6. 8 : Effect of optimised elemental volume v_{el} on the peak temperature

The results show that the optimal arrangement of the elemental volume for the entire structure at this fixed pressure difference should be very small in order to achieve better cooling. Again, Figure 6.9 shows existence of an optimal total number of channels required in the structure. This minimised the peak temperature and also lies in the range of $10 \le N \le 120$.

It is clear from Figures 6.6 to 6.9 that porosity has a significant effect on the peak temperature and the overall thermal resistance. There is no optimum porosity. The

best performance occurs at the highest porosity, which means that as the porosity increases, the peak temperature decreases.

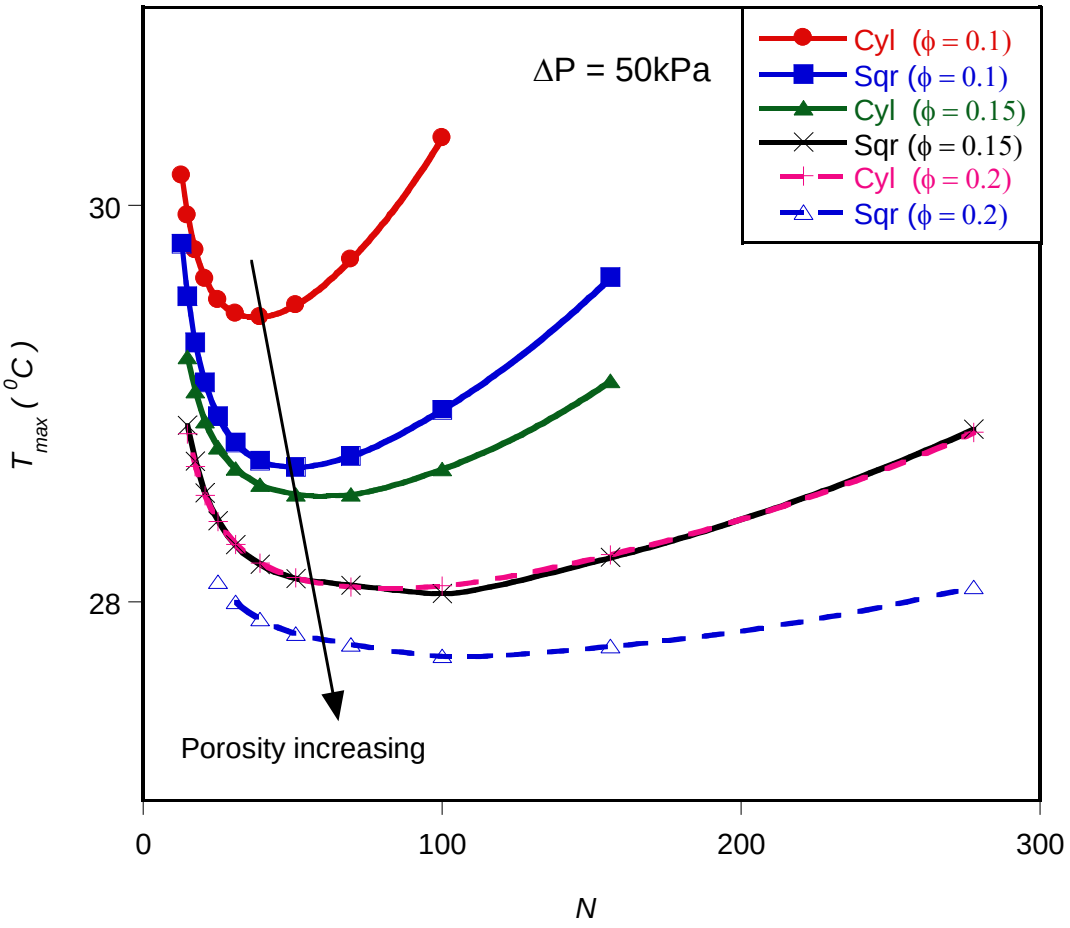

Figure 6. 9： Effect of an optimised total number of channels *N* on the peak temperature

6.2.5. Mathematical formulation of the optimisation problem

The results shown in the preceding session were obtained using a traditional method to post-process the simulation data and results manually. In this section, the entire solution and results are obtained by using a mathematical optimisation algorithm that

searches and identifies the design variables at which the system will perform optimally, since the design variables are mutually interdependent. The approach is to assume that there must be optima design variables at which the system will perform best. A numerical algorithm, Dynamic-Q [208], is employed and incorporated and coupled with the finite volume solver and grid (geometry and mesh) generation package. Figure 6.10 contains a flow chart representing the numerical and optimisation procedure to search and identify the optimal design variables at which the system will perform optimally for greater efficiency and better accuracy. The algorithm is also specifically designed to handle constraint problems where the objective and constraint functions are expensive to evaluate.

The mathematical optimisation algorithm is a multidimensional and robust gradient-based optimisation algorithm that does not require an explicit line search. The details of the Dynamic-Q were discussed in Chapter 4 and it application can also be found in open literature [213-215].

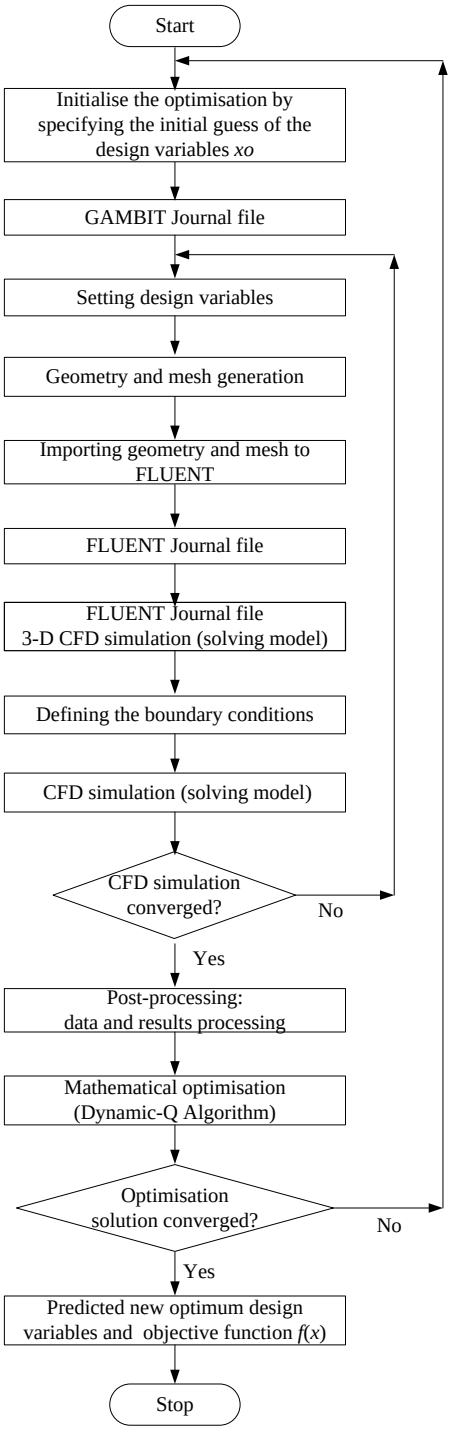

Figure 6. 10 : Flow chart of the numerical simulation process for cooling channels embedded in a high conducting solid

6.2.6. Optimisation problem and design variable constraints

The optimisation technique described above was applied to the models described in Section 6.2.1. The constraint ranges for the optimisation were

$$0.1 \leq \phi \leq 0.2 \tag{6.16}$$

$$0.025\text{mm}^3 \leq v_{el} \leq 5\text{mm}^3 \tag{6.17}$$

$$0 \leq w \leq L \tag{6.18}$$

$$0 \leq d_h \leq w \tag{6.19}$$

and

$$0 \leq s \leq w \tag{6.20}$$

The design and optimisation technique involve the search for and identification of the channel layout that minimises the peak temperature, $T_{\max}$, so that the minimum thermal resistance between the fixed volume and the cooling fluid is obtained with the desired objectives function. This function is not available analytically but it is obtained via a computational fluid dynamic simulation using FLUENT [60].

The hydraulic diameter, channel spacing and elemental volume were considered design variables for the two configurations in the study. A number of numerical optimisations and calculations were carried out within the design constraint ranges given in Equations (6.16) – (6.20), and the results are presented in the next section to show the optimal behaviour of the entire system. The elemental volume of the

structure was in the range of 0.025 mm^3 to 5 mm^3. The optimisation process was repeated for pressure differences across the axial length ranging from 5 kPa to 50 kPa.

6.2.7. Mathematical statement of the optimisation problem

The variables chosen for the mathematical statement are:

$$x_1 = d_h \tag{6.21}$$

$$x_2 = w \tag{6.22}$$

Substituting Equations (6.21) to (6.22) into Equations (6.16) to (6.20) results in the objective and constraints functions given in Equations (6.23) to (6.25). The inequality functions g_1(x) and g_2(x) are derived from the porosity constraint of Equation (6.5). The mathematical statement of the optimisation problem is then written as:

$$f(x) = T_{\max} \tag{6.23}$$

$$g_1(x) = 0.1{x_2}^2 - {x_1}^2 \leq 0 \tag{6.24}$$

$$g_2(x) = {x_1}^2 - 0.2{x_2}^2 \leq 0 \tag{6.25}$$

6.2.8. Parameterisation of geometry and automation of the optimisation process

In order to optimise the performance of the cooling channels, design variables of the geometry should be parameterised because geometric modelling mesh generations are

usually time consuming and labour intensive processes in the analysis computational fluid dynamic problems. The research work requires a large number of CFD simulations to be performed. Therefore, a MATLAB [219] code was developed to read a set of parameters of the geometry. The parameterised code automatically generates GAMBIT [201] and FLUENT script files; runs the scripts and performs post-processing to capture the results in terms of peak temperature as an objective function for different parametric values of each case of configuration studied.

This code starts by reading the parametric values of all the CFD cases and writing GAMBIT and FLUENT journal files for each case. GAMBIT [201] subsequently reads the Gambit journal, generates the mesh and import mesh created into FLUENT for each case. FLUENT [199] then runs the FLUENT journal that reads the corresponding created mesh and sets the model equations, boundary conditions, and solver settings. The FLUENT [199] finally writes maximum peak temperature, as well as mass weighted average and static pressure reports for the boundaries of interest to an output file for each case and process them all so as to calculate final global thermal resistance.

The optimisation problem was done automatically by coupling together the computational fluid dynamics package, FLUENT[199] and the geometry and mesh generation package, GAMBIT [201] with the mathematical optimisation algorithm. The MATLAB [219] code was used so as to allow the automation, mesh generation

and running of the simulation process. This was done by the creation of both GAMBIT [201] and FLUENT [199] journal files, where executed in MATLAB [219] by Windows executable files.

The optimisation algorithm was established by initiating a starting guess value of the design variables. A GAMBIT [58] journal file (*designvariable.jou*) was subsequently written and executed in MATLAB [219]. Another GAMBIT journal file (*CylinderDYNQNEW.jou*) was executed to generate the computational unit geometry mesh while using the geometrical parameters declared by the previous GAMBIT journal file (*designvariable.jou*) operation. The mesh created was imported into FLUENT where simulations and post-processing were carried out by the FLUENT journal file (*fluentDYNQNEW.jou*), Next a temperature data file (*CylinderTemp*.dat) was written stating all the temperatures at the various computational cells. This data file was then read into MATLAB [219], where the maximum temperature was found and equated to the objective function. The DYNAMIC-Q optimisation algorithm provided in Appendix A and written in MATLAB [219] was then used to find better (optimal) design variable vectors where the objective function is achieved. This cycle continued until convergence occurred with the step size and function value convergence tolerances set at 10^{-6} and 10^{-10} respectively. The average time of the simulation and convergence when coupling the FLUENT with mathematical optimisation algorithm for each operating value of dimensionless pressure difference number and configuration was in the range of 12 – 36 hours depending on the channel configuration.

Figure 6.10 provides a flow chart of the automated optimisation process. Appendix B.1 and B.2 show the parametric GAMBIT journal files for geometry with circular and square cooling channels respectively. Appendix C shows the FLUENT journal file according to which simulation was run.

6.2.9. Sensitivity analysis of the selection of forward differencing step size

As discussed in Chapter 4. 6, noise exists in any simulation. It is therefore essential to carefully choose a step size Δx to be used in the differencing scheme carefully so that it reduces the noise and gives an accurate representation of the global gradient of the function. A sensitivity analysis was performed by selecting different values of the step size of design variables that gave a smooth objective function that would later be used as a candidate step size. This candidate step size was then verified by running the optimisation program with various starting guesses and checking for any discrepancies in the final solution. Figure 6.11 shows a graph of peak temperature as a function of the hydraulic diameter of cylindrical cooling channels with step sizes of 10^{-6} and 10^{-4} . Although, different values of the step size of hydraulic diameter as design variable considered are 10^{-6}, 10^{-5}, 10^{-4} and 10^{-3}. A step size of 10^{-4} gives a smooth continuous function of maximum peak temperature and it indeed proved to be an ideal forward differencing scheme step size for other design variables. Figure 6.12 shows a graph of peak temperature as a function of channel spacing with the chosen candidate step size of 10^{-4}.

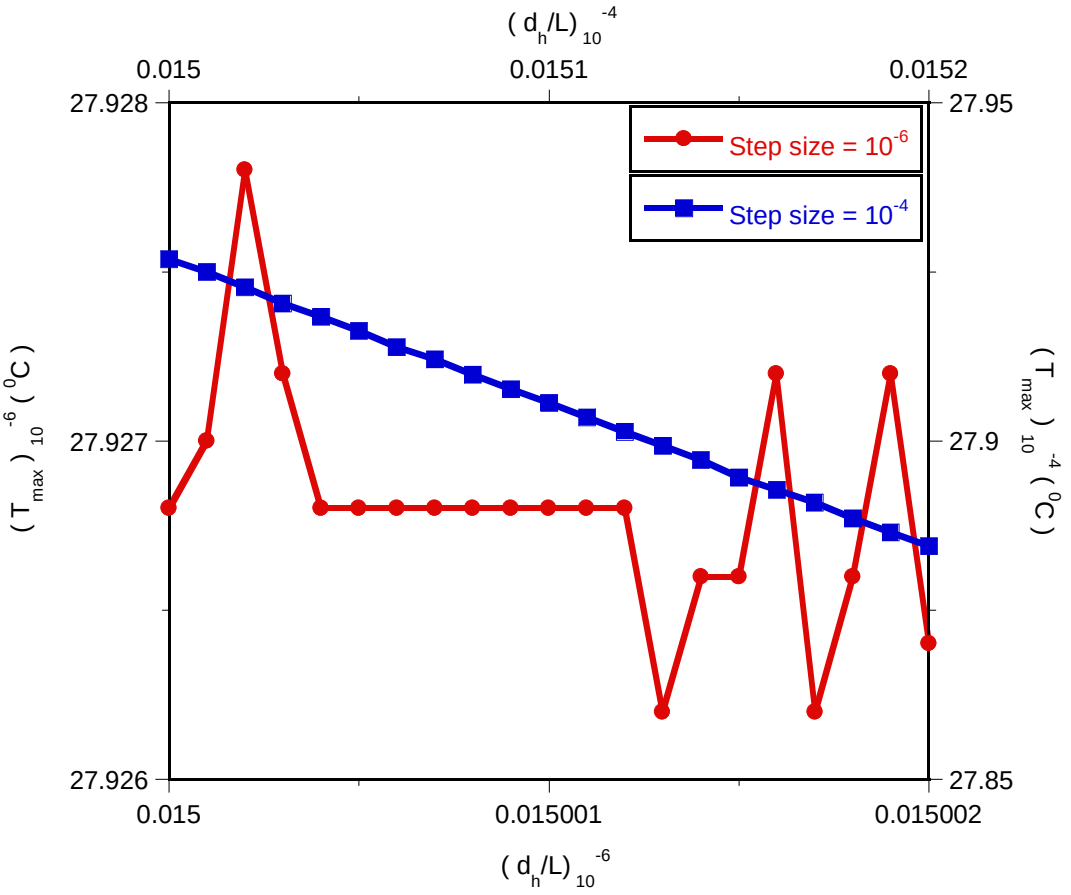

Figure 6. 11 : Plotting of peak temperature for different hydraulic diameter values with step sizes of 10^{-6} and 10^{-4}

Figure 6.13 also shows peak temperature as a function of the hydraulic diameter of square cooling channels with similar sensitivity analysis procedure as for the cylindrical cooling channels. In Figure 6.14 below peak temperature is shown as a function of channel spacing with a candidate step size of 10^{-4}.

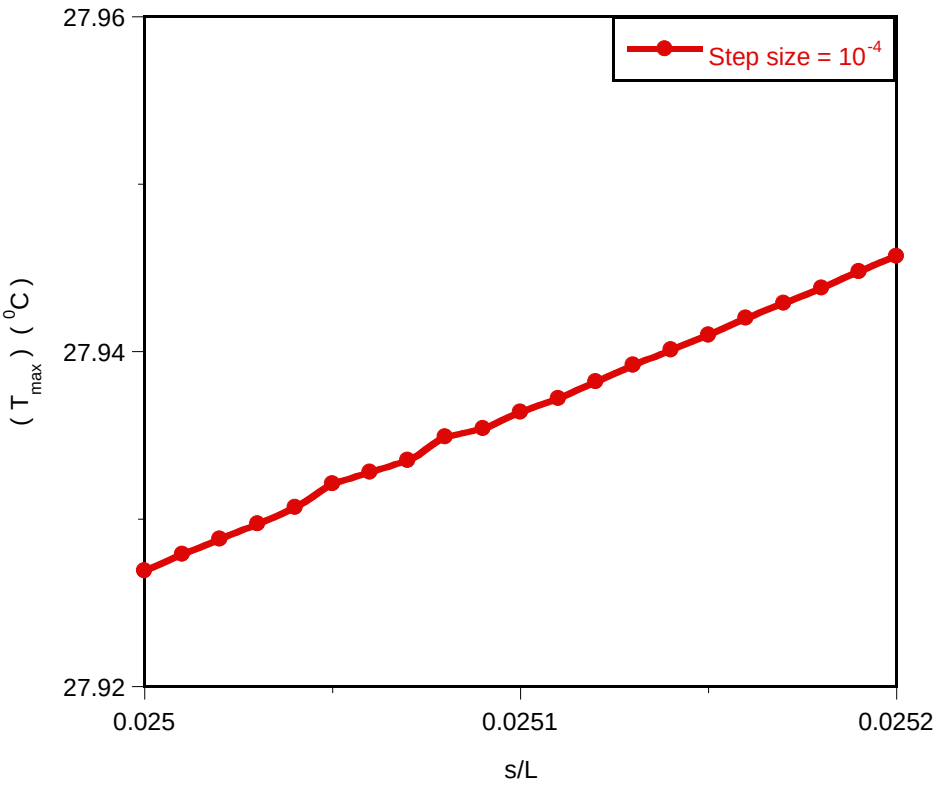

Figure 6. 12 : Plotting temperature for the different channels spacing values with a step size of 10^{-4}

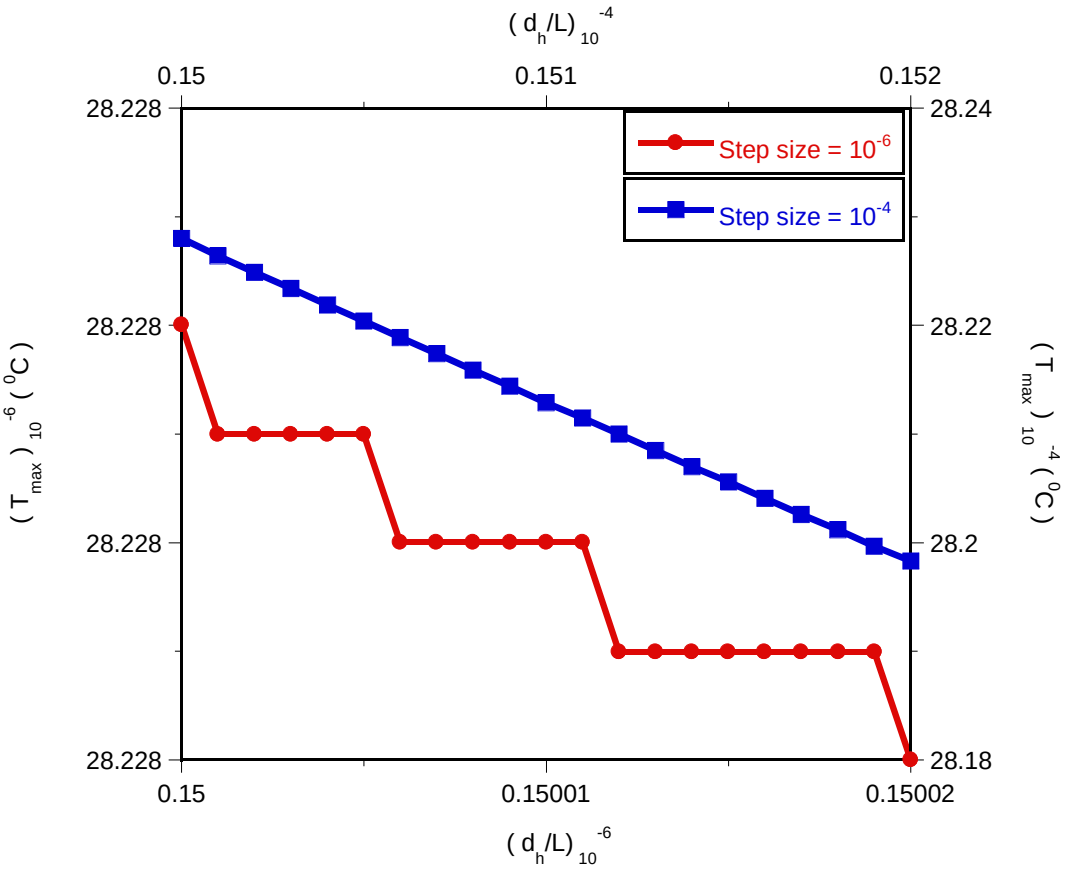

Figure 6. 13 : Plot of temperature for different hydraulic diameter values with step sizes of 10^{-6} and 10^{-4}

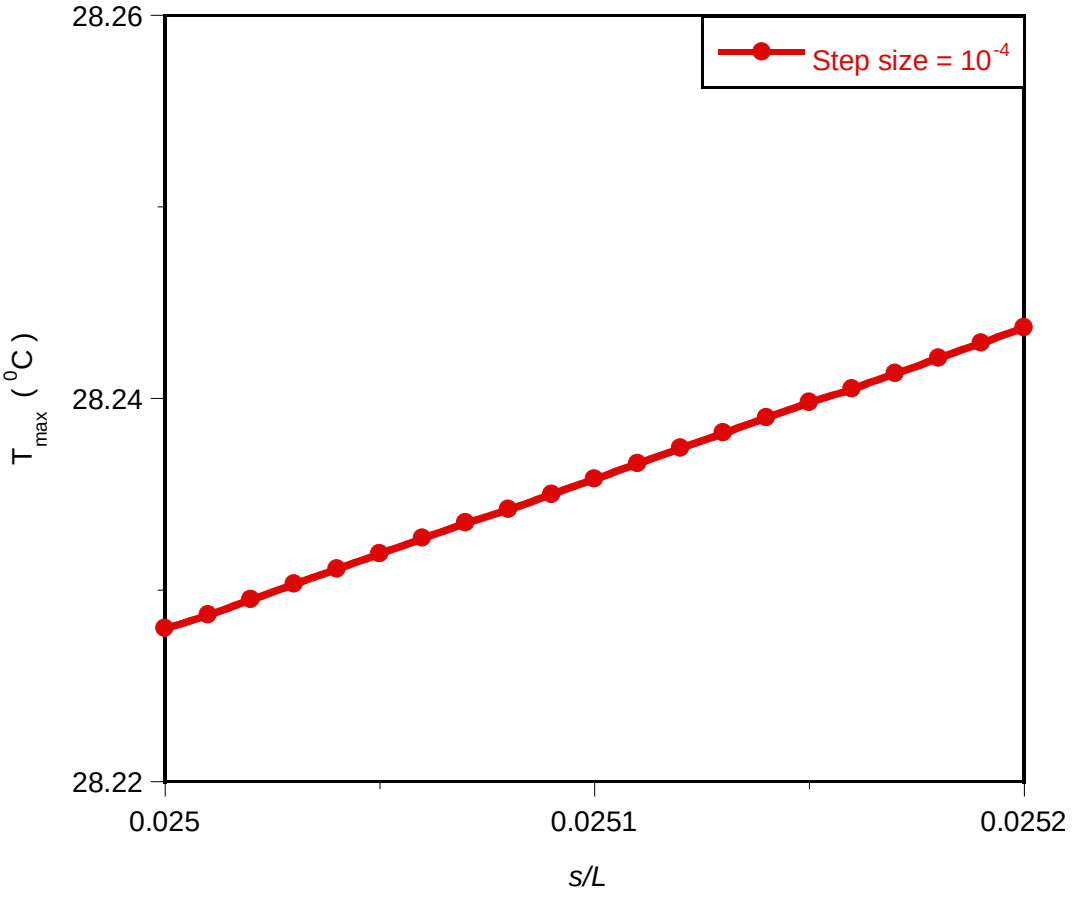

Figure 6. 14 : Plotting temperature for different channels spacing values with a step size of 10^{-4}

6.1.10 Optimisation results

Figure 6.15 shows the optimisation search history of the objective function with respect to iteration for cylindrical configuration in the optimisation searching process by the mathematical optimiser.

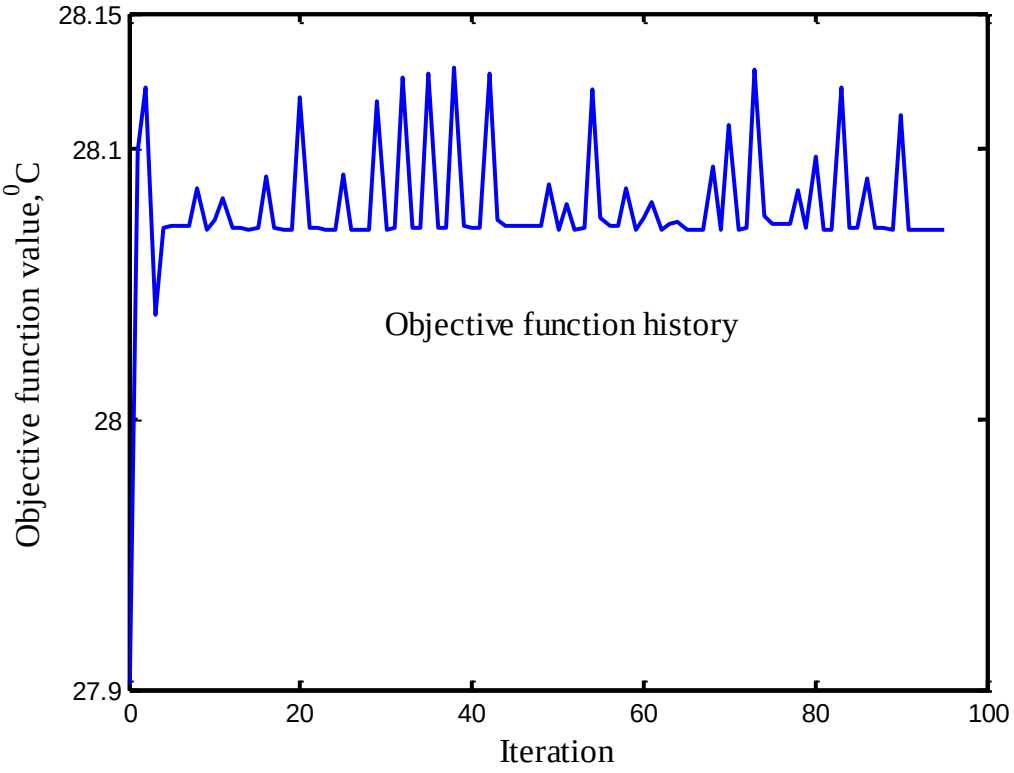

Figure 6. 15 : Objective function history for cylindrical configuration

Figures 6.16 and 6.17 compare the performance of the cooling channel between for the traditional method and mathematical optimiser respectively. Figure 6.16 shows minimised peak temperature curves as a function of pressure drop between the traditional method and the optimiser. The optimised result performs slightly better than the traditional method. The optimisation method relies on the gradients values, and that is why they are more efficient when compared to the traditional method. Figure 6.17 also shows the optimised hydraulic diameter curves. The optimised hydraulic diameter decreases as the pressure difference increases, and the optimised

hydraulic diameter is smaller in the optimisation process than in the traditional method. In the case of the traditional method, the graph shows that when the pressure difference is beyond 30 *kPa*, the pressure difference has no effect on the optimised hydraulic diameter. In contrast, pressure difference slightly influences the optimised shape.

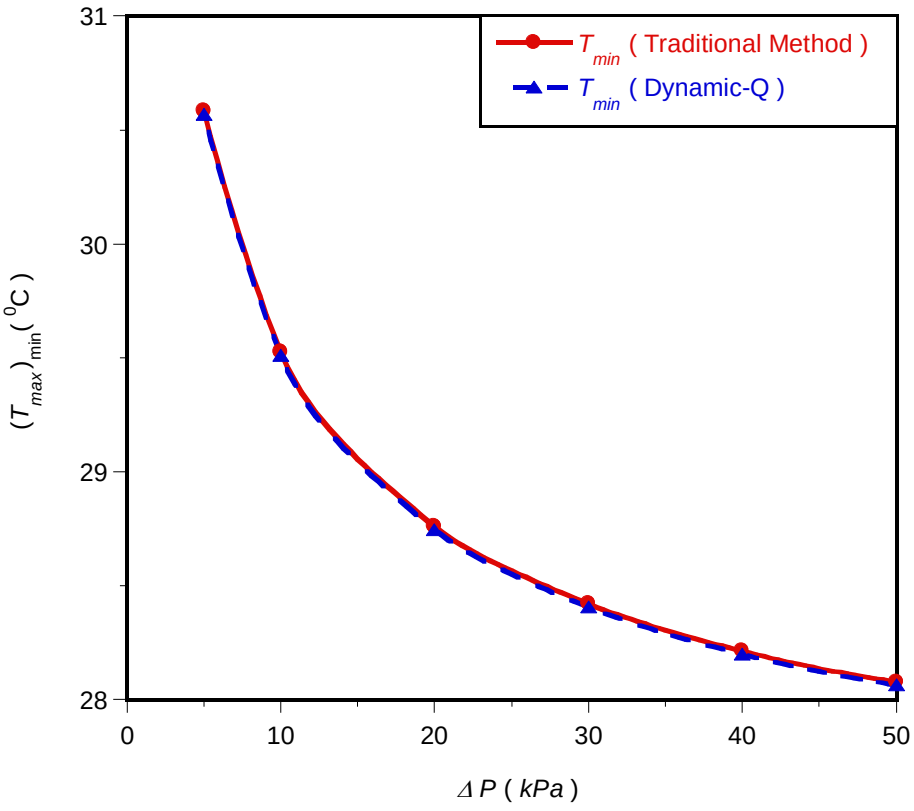

Figure 6. 16 : Comparison of the minimised temperature curves for the traditional method and the optimised cylindrical configuration

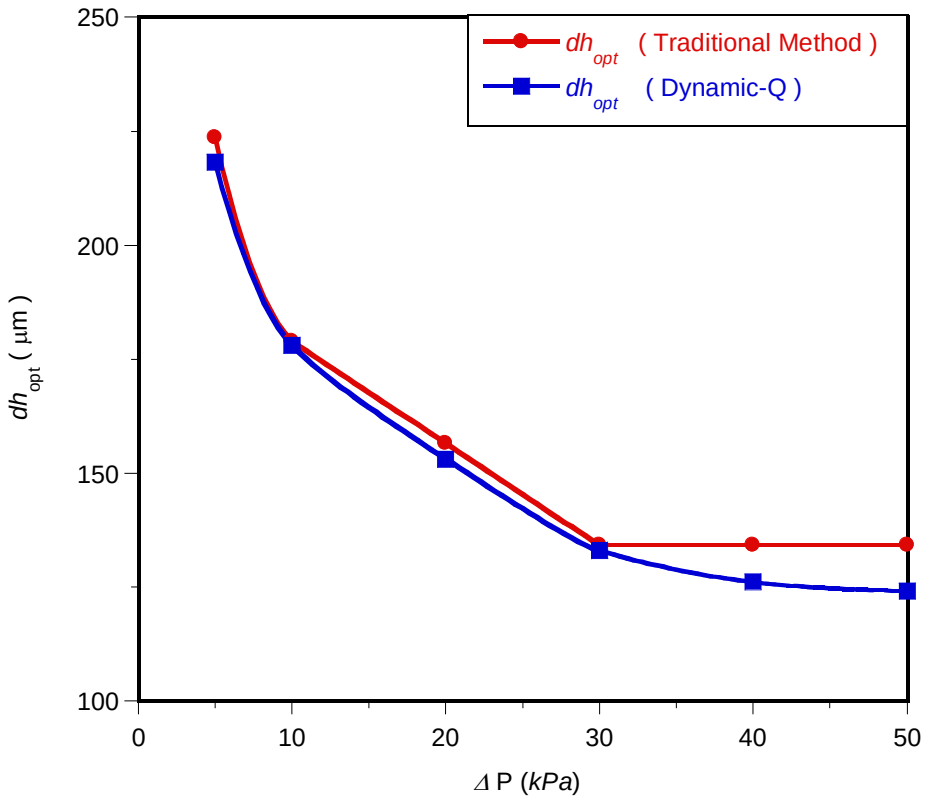

Figure 6. 17 : Comparison of the optimised design variable curves between the traditional method and optimised for cylindrical configuration

6.2.9.1. Effect of applied pressure difference on optimised geometry and minimised thermal resistance

Figure 6.18 shows the effect of the minimised thermal resistance as a function of applied dimensionless pressure difference. Minimised thermal resistance decreases as the applied dimensionless pressure difference number across the axial length and porosity increase. The trend is in agreement with previous work [30].

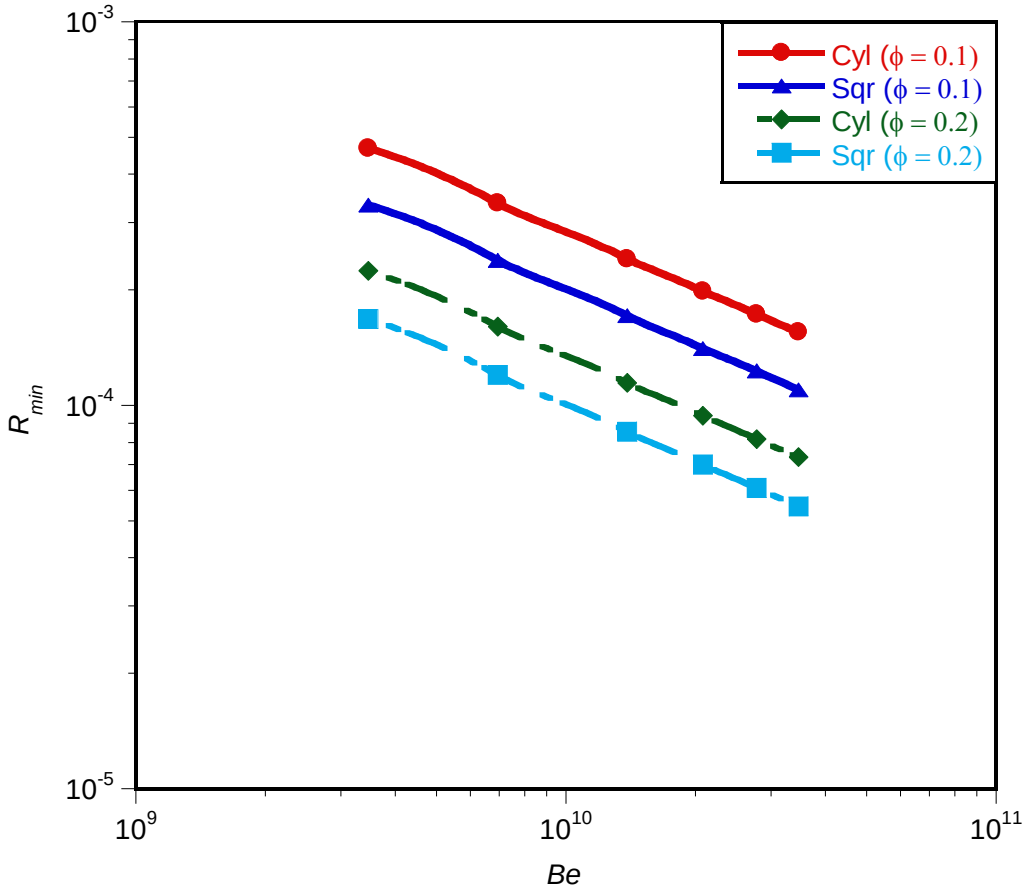

Figure 6. 18 : Effect of dimensionless pressure difference on the dimensionless global thermal resistance

Figure 6.19 shows that there is optima elemental volume for each of the two configurations. It also shows that the optimised global elemental volume decreases as the dimensionless pressure difference increases. Furthermore, there exists a unique optimal elemental volume of geometry for each of the applied pressure differences that minimise the global thermal resistance. This volume lies in the region of $0.5\ \text{mm}^3 \le v_{el} \le 2.4\ \text{mm}^3$. It confirms that the optimal arrangement of the

elemental volume for the entire structure should be very small to achieve better cooling.

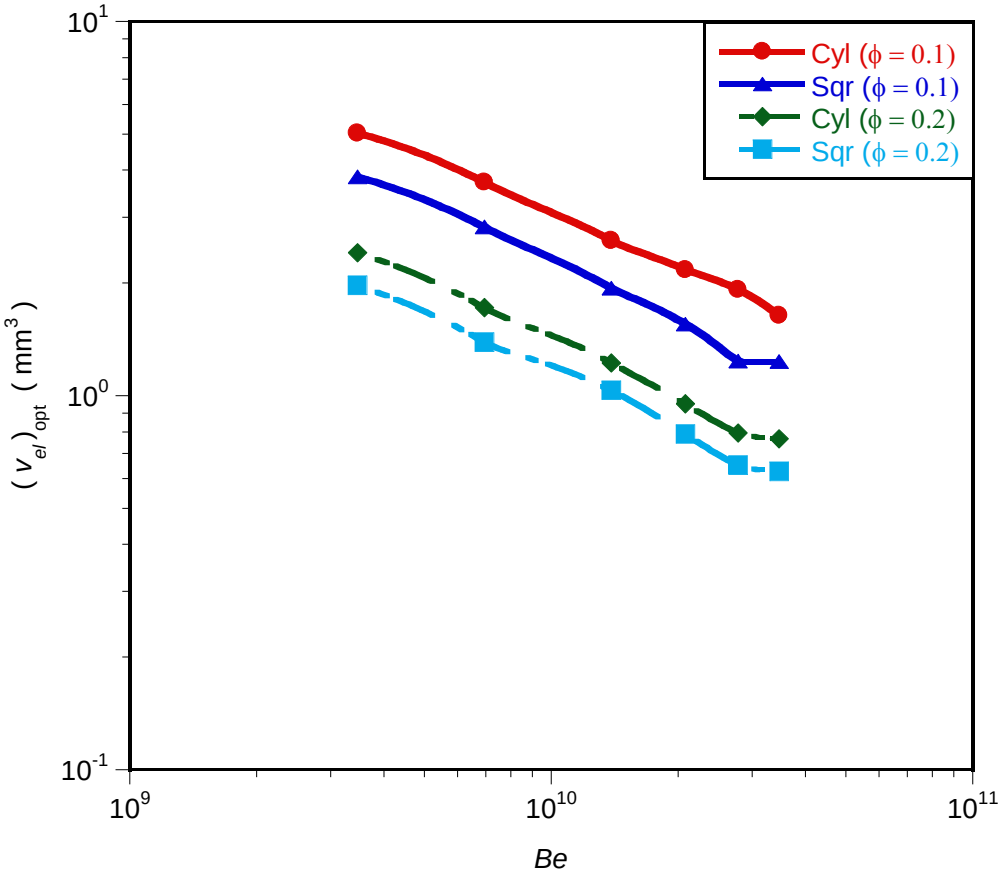

Figure 6. 19 : Effect of dimensionless pressure difference on the dimensionless elemental volume

According to Figure 6.20 the total number of channels (channel arrangement) is a function of pressure difference and porosity increases. The global N_{opt} increases as the pressure difference and porosity increase. N_{opt} lies in the region of $10 \le N_{opt} \le 100$. It is also observed a unique optimal number of channels for every

driving force (*Be*) is required for each configuration so as to achieve effective cooling.

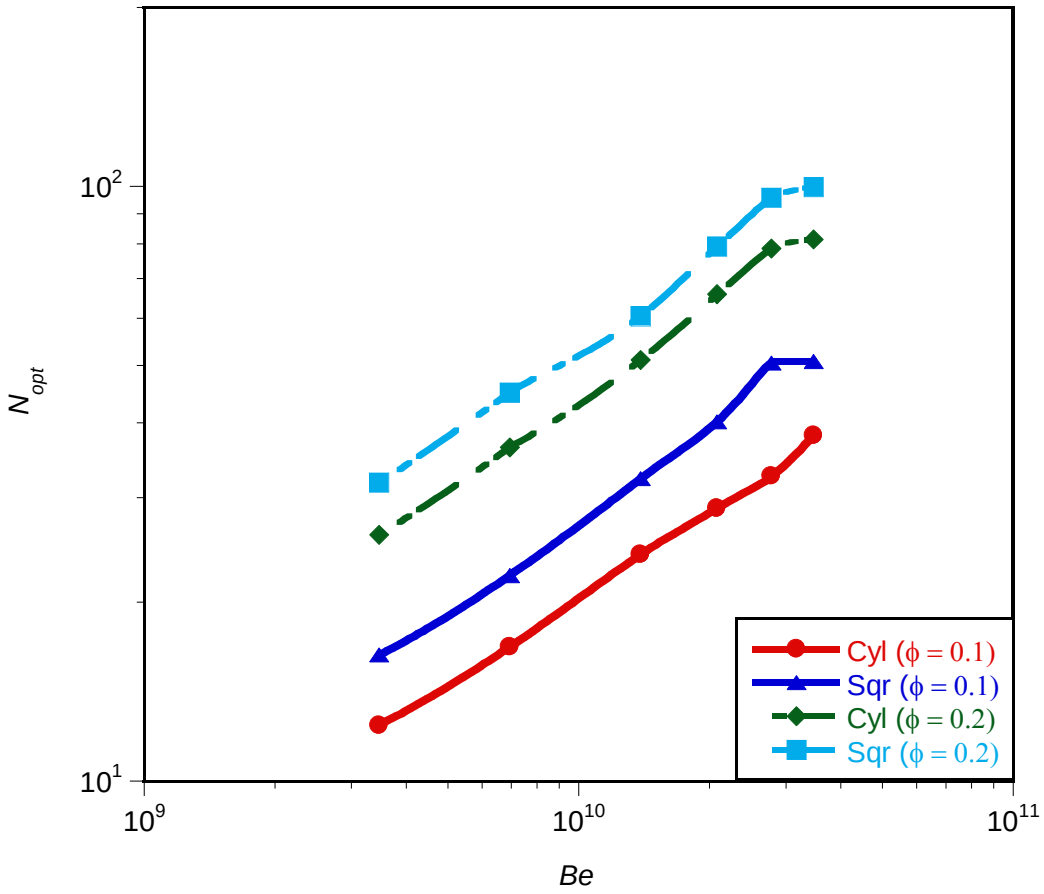

Figure 6. 20 : Effect of dimensionless pressure difference on optimised total number of channels

6.2.10. Comparing the theoretical method and numerical optimisation

6.2.10.1. Effect of dimensionless pressure difference on the minimised dimensionless global thermal resistance

Figure 6.21 shows the minimised dimensionless global thermal resistance as a function of dimensionless pressure difference at optimised design variables for the two configurations. The analytical results of Equations (5.35) and (5.36) validate the numerical solutions. The two optimised solutions have similar trends. Also, the analytical and numerical results show that in the two optimised configurations, the minimised global thermal resistance decreases as the dimensionless pressure difference increases. Although the analytical results are lower than numerical results, the theoretical and numerical values agree within a factor of 1.8 for the worst case. These results are also in agreement with past research work [17, 19, 93].

Equations (6.26) and (6.27) are the correlations for minimised dimensionless thermal resistance and the dimensionless pressure difference for cylindrical and square channels configurations respectively. These are obtained when the geometry is optimised at $\phi = 0.2$ in order to achieve cooling.

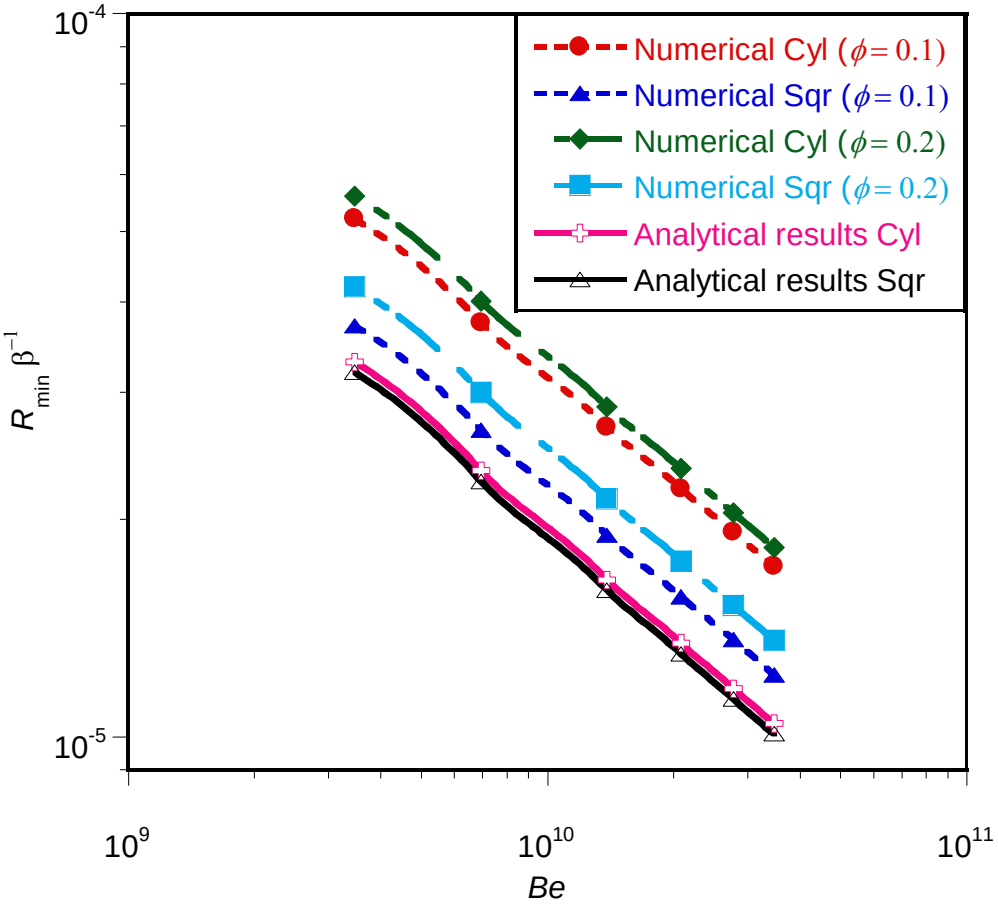

Figure 6. 21 : Correlation of numerical and analytical solutions for the minimised global thermal resistance

$$R_{\min,\,Cyl} = 9.64 Be^{-0.49} \quad , \qquad R^2 = 0.999 \tag{6.26}$$

$$R_{\min,\,Sqr} = 7.68 Be^{-0.49} \quad , \qquad R^2 = 0.999 \tag{6.27}$$

where R^2 is the coefficient of correlation. The correlation given in Equations (6.26) and (6.27) correlate within the error of less than 1% to the CFD results produced.

6.2.10.2. Effect of applied dimensionless pressure difference on optimised design variables

Figures 6.22 and 6.23 show the effect of the dimensionless pressure difference on the optimised hydraulic diameter and channel spacing respectively. The curves show that design variables decrease as applied dimensionless pressure difference and porosity increase.

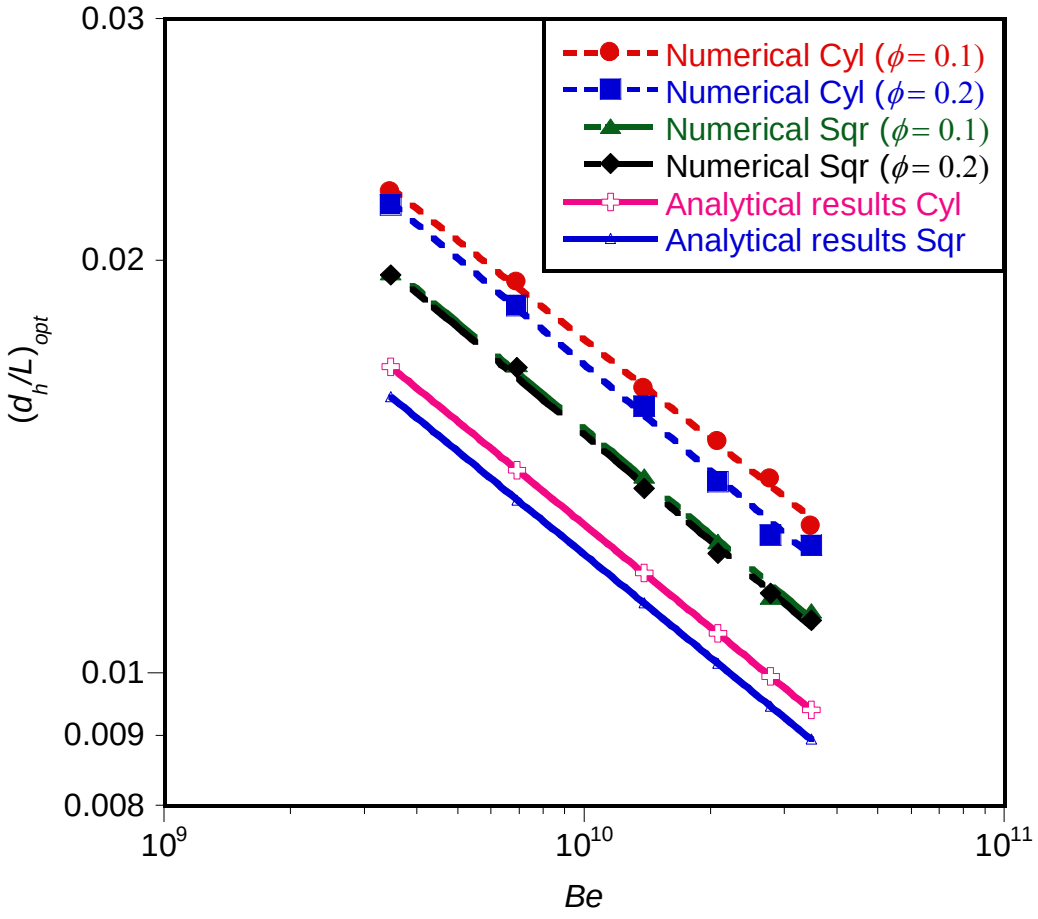

Figure 6. 22 : Correlation between numerical and analytical solutions for the optimised hydraulic diameter

Furthermore, the optimised spacing is directly proportional to the optimised hydraulic diameter. This is also due to the fact that the elemental volume is not fixed, but allowed to morph for a fixed porosity. The graphs also show that, for each configuration, unique optimal design geometries exist for each applied dimensionless pressure number.

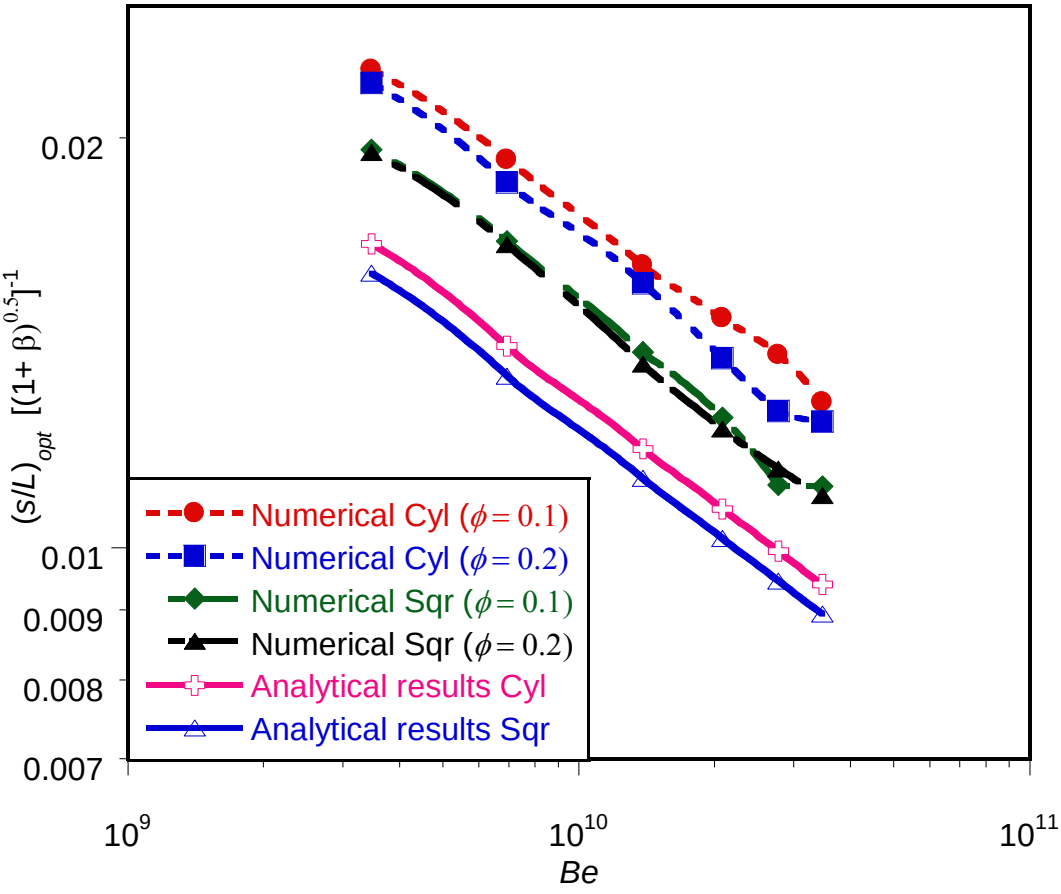

Figure 6. 23 : Correlation beteen numerical and analytical solutions for the optimised spacing

6.2.11. Optimal temperature contours

Figures 6.24(a) and 6.24(b) show the temperature contours of the elemental structure for circular and square configurations, respectively, While Figures 6.24(c) and 6.24(d) show the temperature contours of the inner wall of the cooling channel with cooling fluid for circular and square configurations, respectively. The blue region indicates the region of low temperature and the red region indicates high temperature. The arrow indicates the direction of flow.

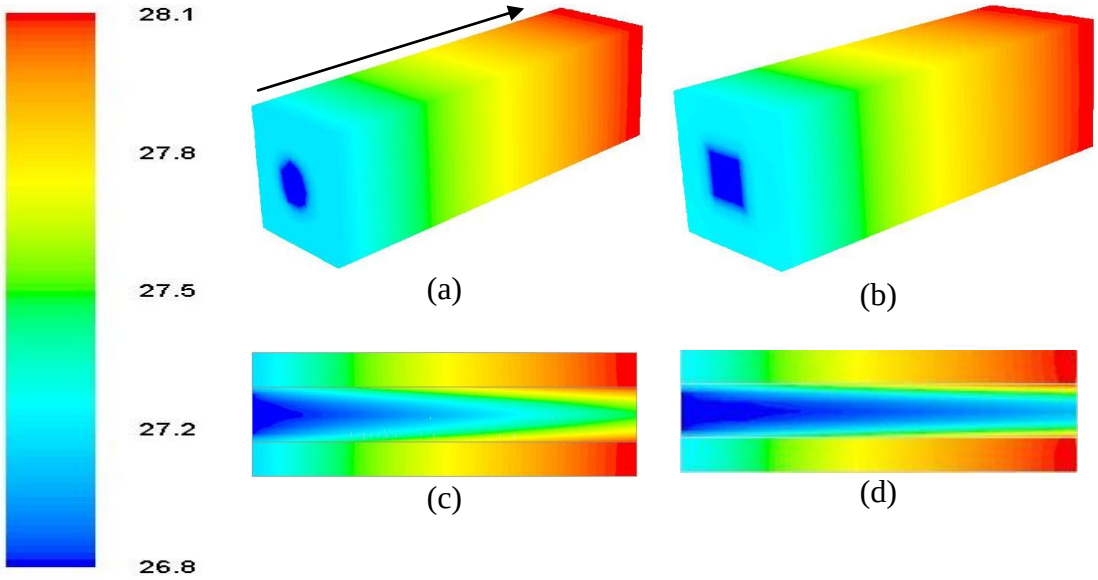

Figure 6. 24 : Temperature distributions on the cooling fluid and inner wall, and unit structure

6.3. CASE STUDY 2: TRIANGULAR COOLING CHANNEL EMBEDDED IN A HIGH-CONDUCTING SOLID

The second case study examines the three-dimensional numerical analysis of thermal resistance in a heat-generated volume. Two types of cross-section channel geometries were used. The first involved equilateral triangles with three equal legs in length and all three internal angles of 60^0. The second was isosceles right triangles with two legs of equal length and internal angles of 90^0, 45^0 and 45^0. Both the equilateral triangle and isosceles right triangle are special case of triangles that can easily and uniformly be packed and arranged to form a larger constructs body, thus minimising the global thermal resistance. A computational elemental volume cell will also be modelled because of the symmetrical heat distribution. The DYNAMIC-Q optimisation algorithm is used to search optimal peak temperatures, hence thermal resistance, by varying the geometric parameters subject to different constraints. The numerical optimisation results obtained that were compared with their analytical solutions in Chapter 5

6.3.1. Computational model

The schematic Figure 5.1(c) in Chapter 5 represents the physical configuration of isosceles right and equilateral triangular cooling channels. The model follows the same principle as that of circular and square configurations in Section 6.2.1.

6.3.1.1. Design variables for isosceles right triangular cooling channels

In Figure 6.25(a), an elemental volume, v_{el}, constraint is considered to be composed of an elemental isosceles right triangular cooling channel of hydraulic diameter, d_h, and the surrounding solid of thickness $s_1$and s_2 at the horizontal and vertical regions respectively. These variables are defined as follows

$$w = h \tag{6.28}$$

$$v_{el} = w^2 L \tag{6.29}$$

$$w = d_h + s \tag{6.30}$$

$$h_c = \frac{w_c}{2} \tag{6.31}$$

$$b = \frac{\sqrt{2}}{2} w_c \tag{6.32}$$

$$d_h = \frac{w_c^{\,2}}{w_c + \sqrt{2} w_c} \tag{6.33}$$

$$v_c = \frac{w_c^{\,2}}{4} L \tag{6.34}$$

However, the void fraction or porosity of the unit structure can be defined as

$$\phi = \frac{v_c}{v_{el}} = \frac{1}{4}\left(\frac{w_c}{w}\right)^2 \tag{6.35}$$

6.3.1.2. Design variables for equilateral triangular cooling channels

Again, in Figure 6.25(b), an elemental volume, v_{el}, constraint is considered to be composed of an elemental equilateral triangular cooling channel of hydraulic diameter, d_h, and the surrounding solid of thickness $s_1$and s_2 at the horizontal and vertical regions respectively. These variables are defined as follows

$$w = h \tag{6.36}$$

$$v_{el} = w^2 L \tag{6.37}$$

$$w = d_h + s \tag{6.38}$$

$$h_c = \frac{\sqrt{3}}{2} w_c \tag{6.39}$$

$$d_h = \frac{1}{\sqrt{3}} w_c \tag{6.40}$$

$$v_c = \frac{\sqrt{3}}{4} w_c^{\,2} L \tag{6.41}$$

However, the void fraction or porosity of the unit structure can be defined as

$$\phi = \frac{v_c}{v_{el}} = \frac{\sqrt{3}}{4} \left(\frac{w_c}{w} \right)^2 \tag{6.42}$$

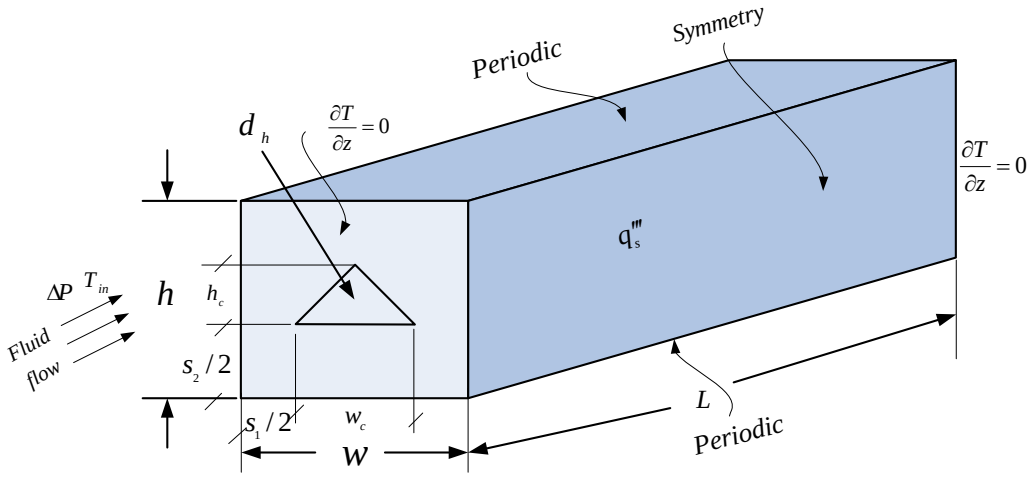

(a)

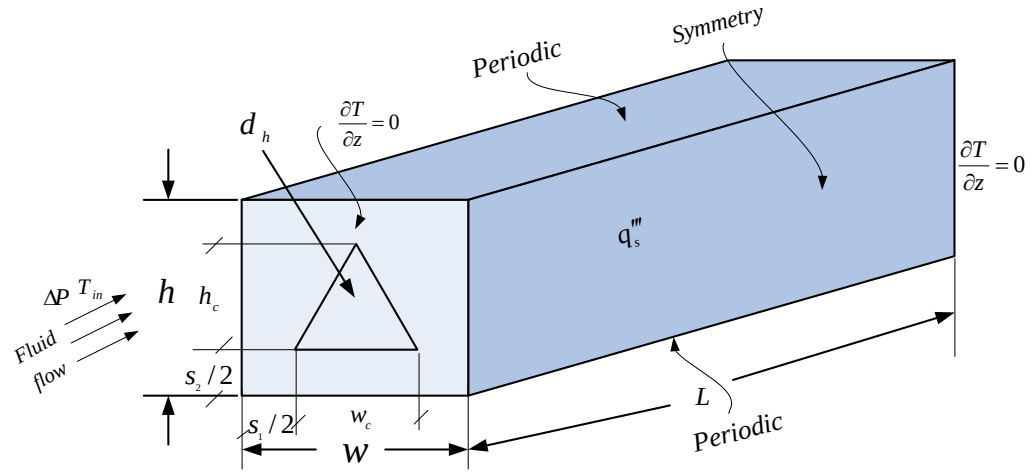

(b)

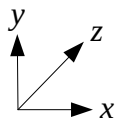

Figure 6. 25 : The boundary conditions of the three-dimensional computational domain for (a) isosceles right triangular cooling channels and (b) equilateral triangular cooling channels

Therefore, the total number of channels in the structure arrangement for the two triangular configurations can be defined as:

$$N = \frac{HW}{hw} = \frac{HW}{(h_c + s_2)(w_c + s_1)} \tag{6.43}$$

The temperature distribution in the model was determined by solving the equation for the conservation of mass, momentum and energy numerically. The discretised three-dimensional computational domain representing the two triangular configurations is shown in Figure 6.26. The cooling fluid was water; it is assumed to be in single-phase, steady, and a Newtonian fluid with constant thermo-physical properties, and was forced through the cooling channels by a specified pressure difference, ΔP across the axial length of the structure.

Also, other assumptions imposed on the triangular configurations are, the solid structure top and bottom boundaries of the domain correspond to periodic boundary conditions, the left and right side of the solid surfaces were taken as symmetry boundary conditions. All the outside walls were taken as plane of symmetry of the solid structure and were modelled as adiabatic as shown in Figure 6.25.

The objective function here is the minimum global thermal resistance which has been expressed in a dimensionless form in equation (6.13) and it is a function of the optimised design variables and the peak temperature. that is:

$$R_{\min} = f\left(AR_{c_{opt}},\ d_{h_{opt}},\ s_{1_{opt}},\ s_{2_{opt}},\ v_{el_{opt}},\ T_{\max_{\min}}\right) \tag{6.44}$$

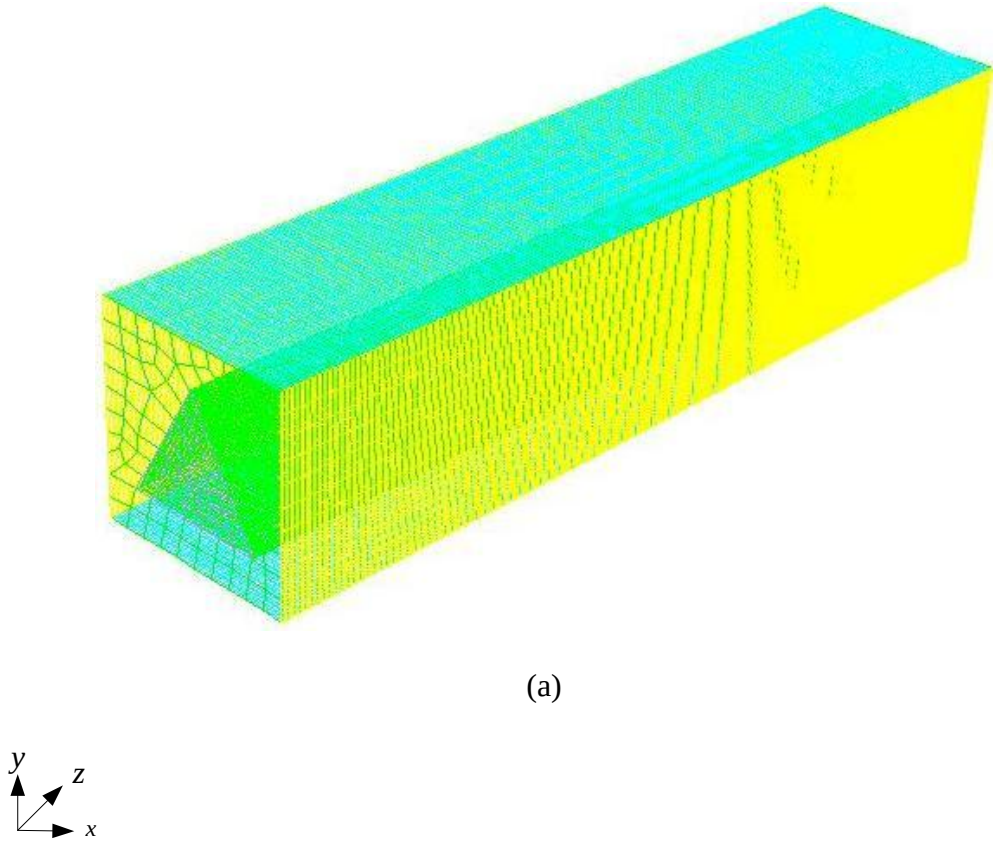

(a)

Figure 6. 26 : The discretised 3-D computational domain for triangular cooling channel

6.3.2. Numerical procedure

The procedure for numerical simulation used here is the same with little modification to that of circular and square configurations discussed in Section 6.2.2. It began by fixing the length of the channel, applied pressure difference, porosity, internal heat generation and material properties. We kept varying the values of elemental volume and hydraulic diameter or base length of the channel in order to identify the best (optimal) geometries that minimised the peak temperature.

The numerical solutions of the continuity, momentum and energy equations (Equations (3.1) to (3.8) of Chapter 3) along with the boundary conditions (Equations (6.6) to (6.12)) were obtained over the discretised domain shown in Figure 6.21 for the two triangular configurations. A three-dimensional finite volume commercial package FLUENT™ [199] was used, coupled with the geometry and mesh generation package GAMBIT [201] and MATLAB [219]. The GAMBIT [201] journal files for the isosceles right and equilateral triangular configurations are supplied in Appendixes B.3 and B.4 respectively. FLUENT [199] journal file in Appendix C is applicable to the simulations with little modification.

6.3.3. Grid analysis and code validation

To ensure accurate results, several grid independence tests were conducted until a mesh size with negligible changes in peak temperature was obtained. Tables 6.1 and 6.2 show the grid independence test for isosceles right triangular and equilateral triangular configurations with $v_{el} = 0.4\ \text{mm}^3$ $\phi = 0.2$, $L = 10\ \text{mm}$ for $\Delta P = 50\ kPa$. Also, computational cells densities of 32 526, 59 000 and 76 728 were used for the grid independence test for an isosceles right triangular configuration. It was observed that almost identical results were predicted when 59 000 and 76 728 cells were used. Therefore, any increase in the cell density beyond 59 000 had a negligible effect on the numerical result.

Again, computational cells densities of 33 360 63 500 and 77 284 were used for the grid independence test for the equilateral triangular configuration. It was observed that almost identical results were predicted when 63 500 and 77 284 cells were used. A further increase in the cell density beyond 63 500 would have a negligible effect on the numerical result.The convergence criterion for the overall thermal resistance as the quantity monitored is given in Equation (6.15).

Table 6. 1 : Grid independence study for the isosceles right triangular configuration with $v_{el} = 0.4\ \text{mm}^3$ $\phi = 0.2$ **and** $\Delta P = 50\ kPa$

Number of nodes	Number of cells	$T_{\max}$	$\gamma = \frac{\left\|(T_{\max})_i - (T_{\max})_{i-1}\right\|}{\left\|(T_{\max})_i\right\|}$
45 950	32 526	27.89944	-
79 120	59 000	27.94366	0.001582
101 332	76 728	27.96155	0.00064
150 190	118 750	27.99271	0.001113

Table 6. 2 : Grid independence study for the equilateral triangular configuration with $v_{el} = 0.4\ \text{mm}^3$ $\phi = 0.2$ **and** $\Delta P = 50\ kPa$

Number of nodes	Number of cells	$T_{\max}$	$\gamma = \frac{\left\|(T_{\max})_i - (T_{\max})_{i-1}\right\|}{\left\|(T_{\max})_i\right\|}$
28 034	1 9 314	27.81091	-
46 786	33 360	27.8580	0.00169
83 629	63 500	27.90048	0.001523
101 889	77 284	27.91846	0.000644

6.3.4. Numerical results

In this section, we present results for the case when the elemental volume was in the range of $0.025\ \text{mm}^3 \le v_{el} \le 5\ \text{mm}^3$ and the porosities ranged between $\phi = 0.2$ with a fixed length of L = 10 mm and fixed applied dimensionless pressure differences of $\Delta P = 50$ kPa. The internal heat generation within the solid was taken to be fixed at 100 kW/m^3.

Figures 6.27 and 6.28 show the existence of an optimal hydraulic diameter and optimal elemental volume of the structure that minimised the peak temperature at any point in the channel for the two types of triangular configurations studied. The abbreviation (E-T) is used for equilateral triangle and (I-T) is used for isosceles right triangle. Figure 6.27 shows the peak temperature as a function of the channel dimensionless hydraulic diameter for prescribed pressure difference. It shows that there exists an optimal channel hydraulic diameter, which lies in the range $0.005 \le d_h/L \le 0.02$ and minimises the peak temperature. Also, the elemental volume of the structure has a strong effect on the peak temperature as shown in Figure 6.28. The minimum peak temperature is achieved when the optimal elemental volume of the structure minimises the peak temperature and this lies in the range of $0.2\ \text{mm}^3 \le v_{el} \le 2.5\ \text{mm}^3$. Any further increase or decrease in the design variable beyond the optimal values indicates that the working fluid is not properly engaged in the cooling process. This is detrimental to the global performance of the system. The results also, show

that the optimal arrangement of the elemental volume for the entire structure at this fixed pressure difference should be very small in order to achieve better cooling.

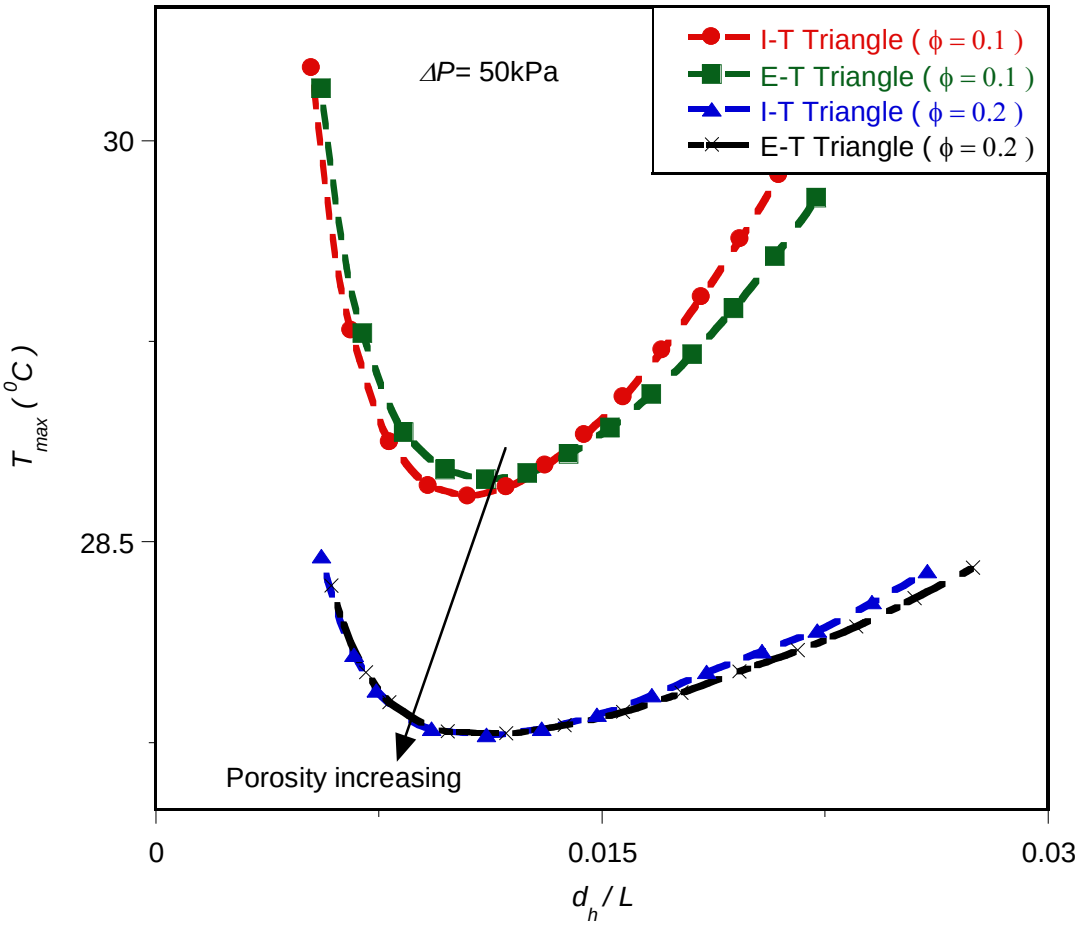

Figure 6. 27 : Effect of the optimised hydraulic diameter d_h on the peak temperature

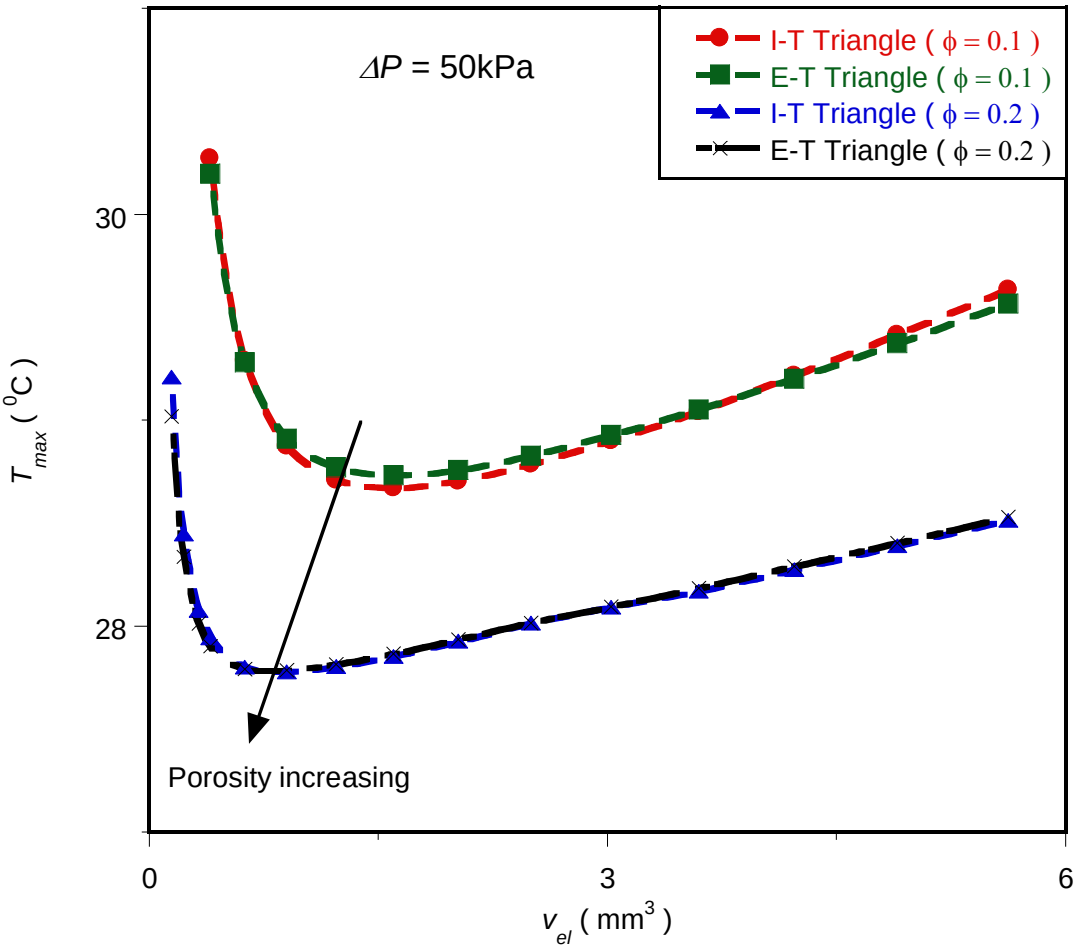

Figure 6. 28 : Effect of optimised elemental volume, v_{el} on the peak temperature

6.3.5. Mathematical formulation of the optimisation problem

In this section, we also introduce an DYNAMIC-Q algorithm that will search and identify the optimal design variables at which the system will perform at an optimum. the objective function is the minimisation of global thermal resistance.

6.3.5.1. Optimisation problem and design variable constraints

The optimisation technique described in Section 6.2.5 was applied to the triangular models described in Section 6.3.1.

The constraint ranges for the two triangular configurations are

$$0.1 \leq \phi \leq 0.2 \tag{6.45}$$

$$0.025\text{mm}^3 \leq v_{el} \leq 5\text{mm}^3 \tag{6.46}$$

$$h_c = w_c \tag{6.46}$$

$$0 \leq w_c \leq w \tag{6.48}$$

$$0 \leq d_h \leq w \tag{6.49}$$

And

$$0 \leq s_1 \leq w \tag{6.50}$$

$$0 \leq s_2 \leq w \tag{6.51}$$

The optimisation process was repeated for pressure differences across the axial length ranging from 5 kPa to 50 kPa within the design constraint ranges given in Equations (6.45) to (6.51). This was done in order to search for and identify the channel layout that minimises the peak temperature $T_{\max}$ so that the minimum thermal resistance between the fixed volume and the cooling fluid is obtained as the desired objectives function

6.3.6. Mathematical statement of the optimisation problem

The variables chosen for the mathematical statement are:

$$x_1 = w_c \tag{6.52}$$

$$x_2 = w \tag{6.53}$$

Substituting Equations (6.52) and (6.53) for Equations (6.45) to (6.51) results in the objective and constraints functions given in Equations (6.54) to (6.56) and in Equations (6.57) to (6.59) for isosceles right and equilateral triangular configurations respectively. The inequality functions g_1(x) and g_2(x) are derived from the porosity constraint of Equations (6.35) and (6.42) for isosceles right and equilateral configurations respectively.

Therefore, the mathematical statement of the optimisation problem for an isosceles right triangular configuration can then be written as:

$$f(x) = T_{\max} \tag{6.54}$$

$$g_1(x) = 0.4x_2^{\,2} - x_1^{\,2} \le 0 \tag{6.55}$$

$$g_2(x) = x_1^{\,2} - 0.8x_2^{\,2} \le 0 \tag{6.56}$$

Also the mathematical statement of the optimisation problem for an equilateral triangular configuration can be written as

$$f(x) = T_{\max} \tag{6.57}$$

$$g_1(x) = \frac{0.4}{\sqrt{3}} x_2^{\,2} - x_1^{\,2} \leq 0 \tag{6.58}$$

$$g_2(x) = x_1^{\,2} - \frac{0.8}{\sqrt{3}} x_2^{\,2} \leq 0 \tag{6.59}$$

6.3.7. Sensitivity analysis of the selection of forward differencing step size

Figure 6.29 shows a graph of the peak temperature as a function of the structure width of isosceles right triangular cooling channels, with a similar sensitivity analysis procedure for cylindrical cooling channel with step sizes of 10^{-6} and 10^{-4}. Although, different values of the step size of structure width as design variable considered are 10^{-6}, 10^{-5}, 10^{-4} and 10^{-3}. Figures 6.30 shows a graph of the peak temperature as a function of channel hydraulic diameter with a candidate step size of 10^{-4}.

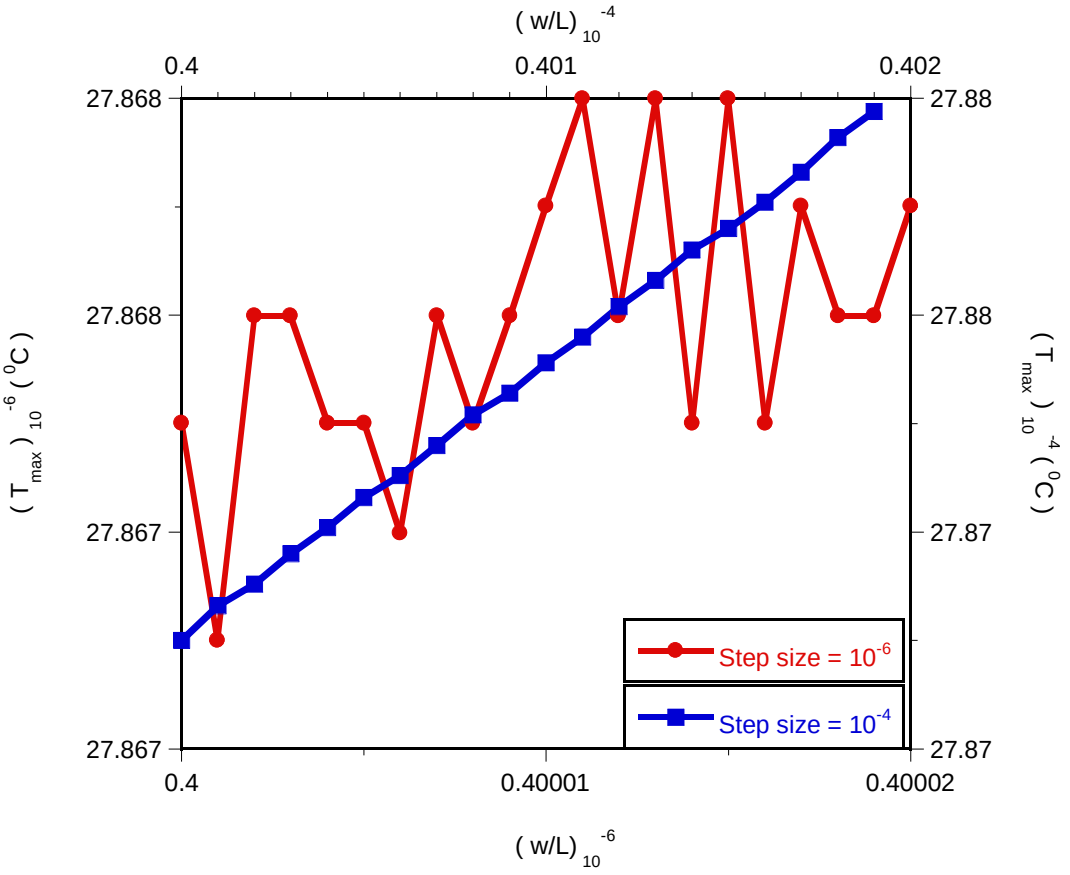

Figure 6. 29 : Plotting temperature for different structure width values with step sizes of 10^{-6} and 10^{-4}

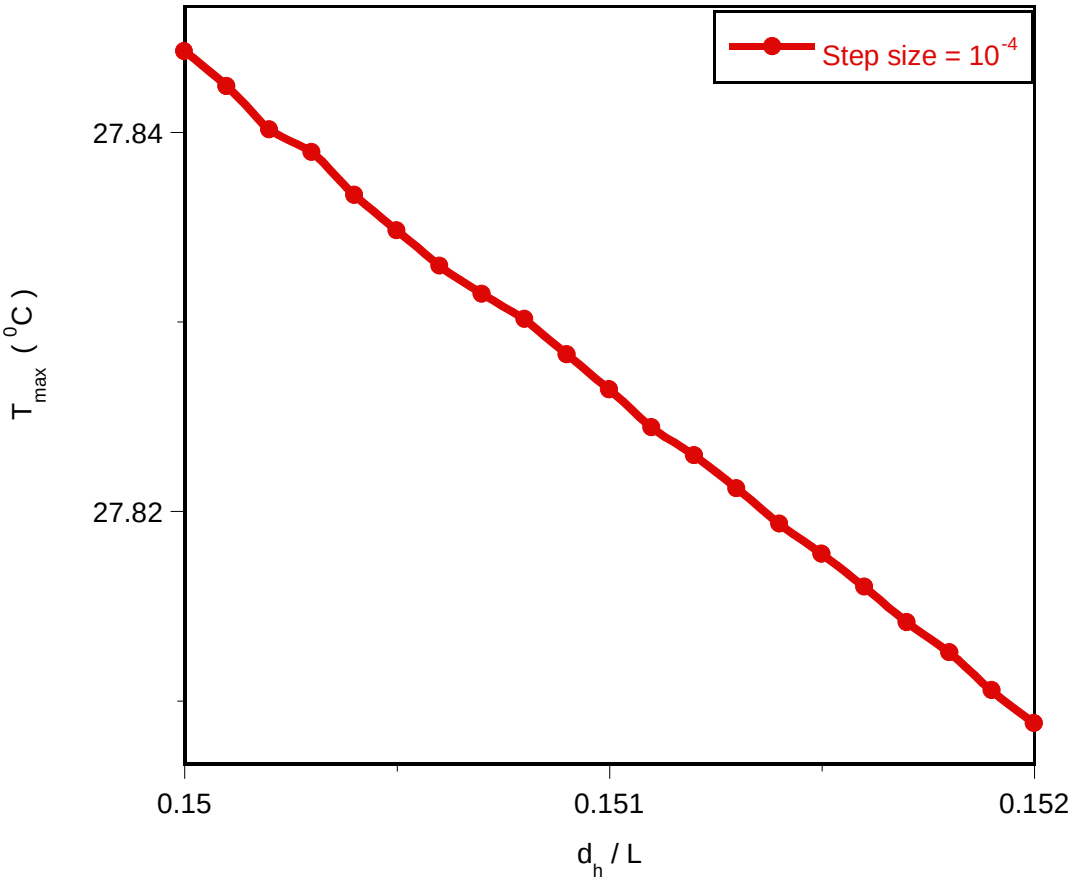

Figure 6. 30 : Plotting temperature for different hydraulic diameter values with a step size of 10^{-4}

6.3.8. Optimisation results

6.3.8.1. Effect of applied pressure difference on optimised geometry and minimised thermal resistance

Figure 6.31 shows the effect of the minimised thermal resistance as a function of applied dimensionless pressure difference. Minimised thermal resistance decreases as

the applied dimensionless pressure difference across the axial length and porosities increase. This trend is in agreement with previous work [94].

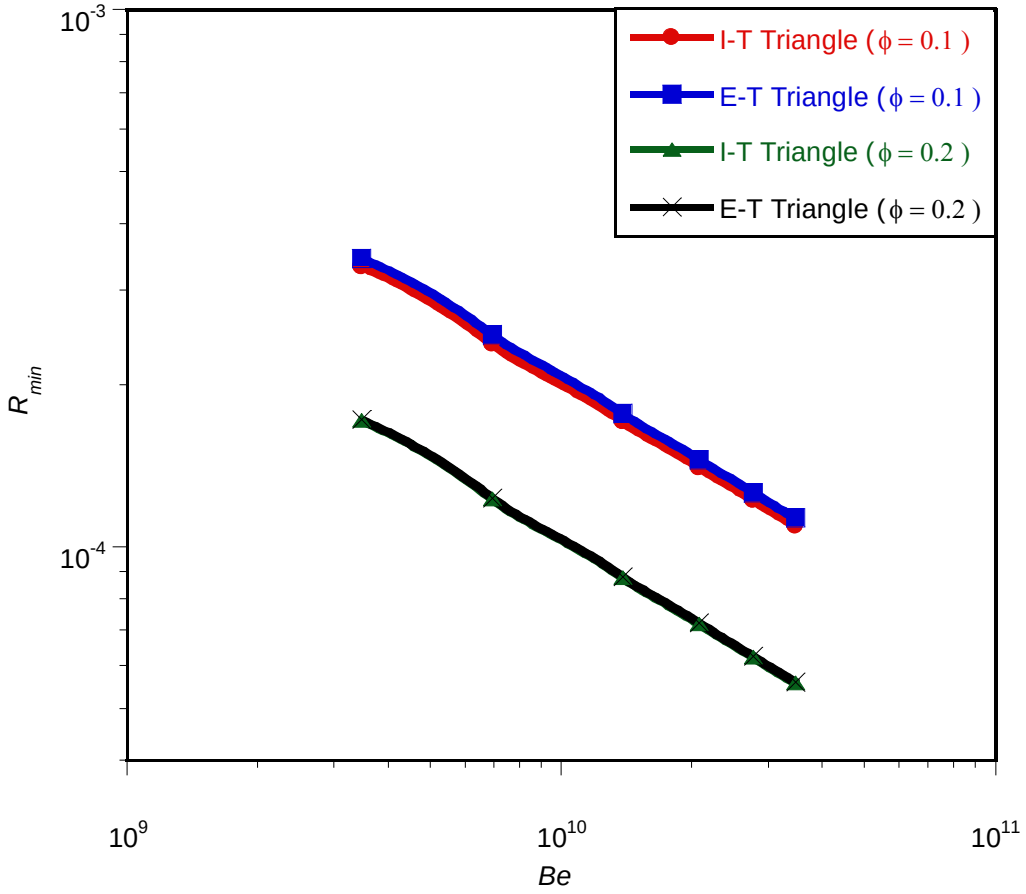

Figure 6. 31 : Effect of dimensionless pressure difference on the minimised global thermal resistance

Also, Figures 6.32 and 6.33 show the optimal behaviours of the geometry with respect to the applied dimensionless pressure difference number (or Bejan number) at different porosity for the two triangular configurations. Figure 6.32 shows that the optimal hydraulic diameter decreases as the dimensionless pressure differences increase. There also exists a unique optimal geometry for each of the applied

dimensionless pressure differences for the configurations. Figure 6.33 shows that the optimal channel spacing ratio (s_1/s_2) remains unchanged regardless of the dimensionless pressure difference number. This constant value could be described as allowable spacing due to manufacturing constraints. It implies that the closer the channels are to one another, the better the effective cooling ability of the global system.

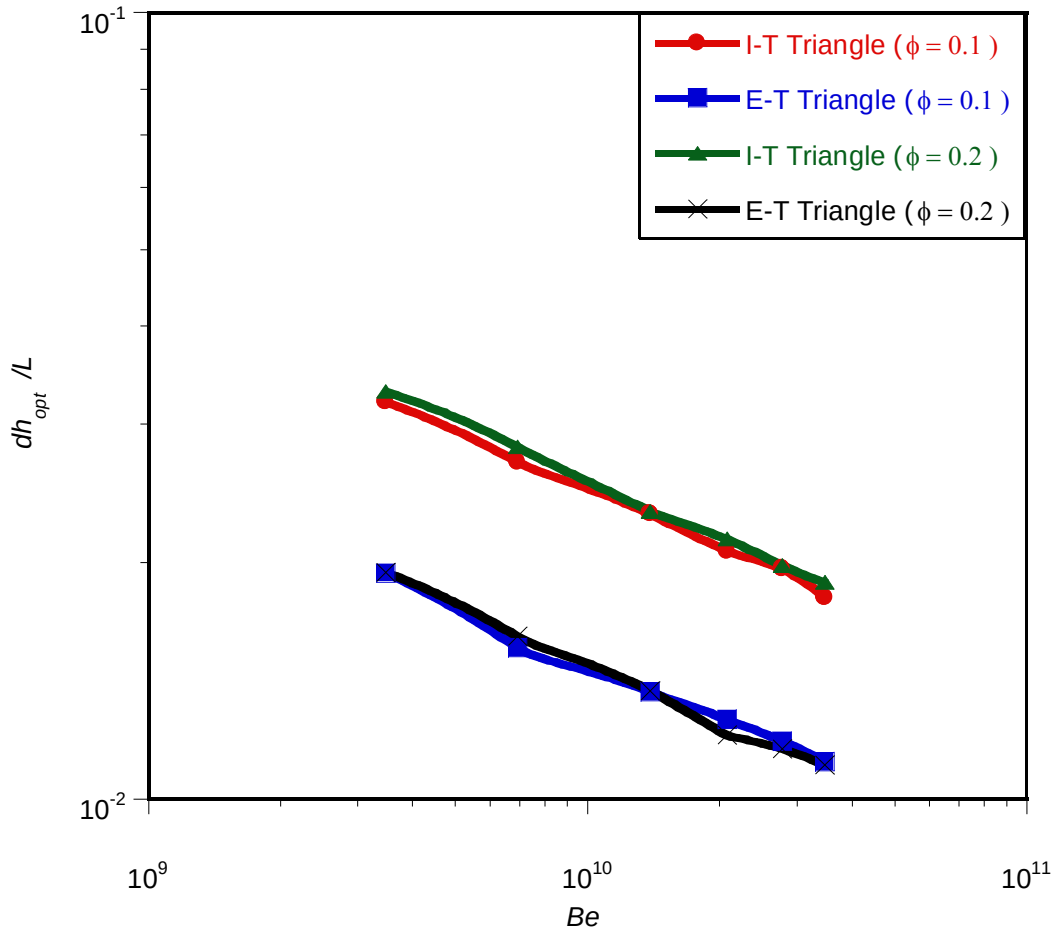

Figure 6. 32 : Effect of dimensionless pressure difference on the optimised hydraulic diameter

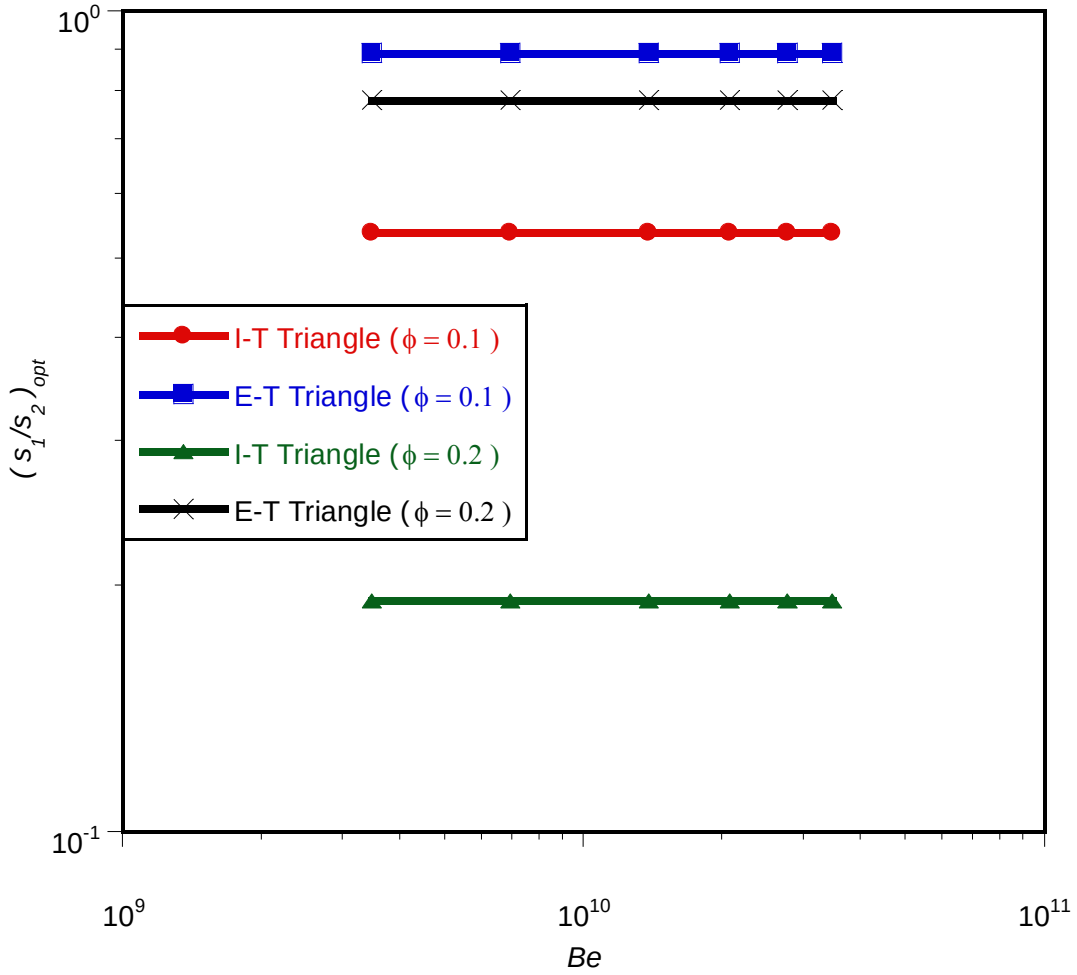

Figure 6. 33 : Effect of dimensionless pressure difference on the optimised channel spacing ratio

6.3.9. Comparison of the theoretical method and numerical optimisation

6.3.9.1. Effect of dimensionless pressure difference on the minimised dimensionless global thermal resistance

The analytical results of Equations (5.37) and (5.38) were used to validate the numerical solutions. The numerical and approximate solutions, based on scale analysis at optimal geometry dimensions, are in good agreement and the solutions follows similar trends as shown in Figure 6.34. Although the analytical results are lower than numerical results, the theoretical and numerical values agree within a factor of 1.5 for the worst case. However, these deviations are attributed to simplifying assumptions made in the formulation of the theoretical solution. These results are also in agreement with past research work [17, 93].

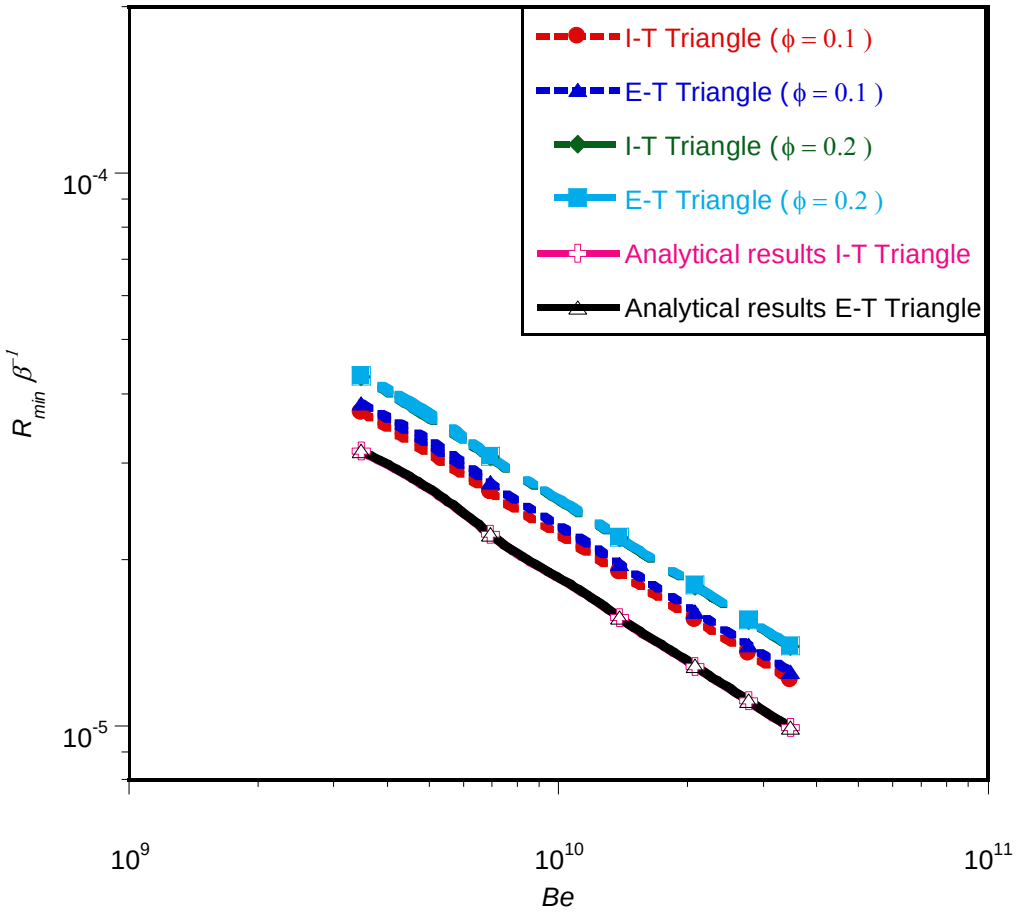

Figure 6. 34 : Correlation between the numerical and analytical solutions for the minimised global thermal resistance

Equations (6.60) and (6.61) are the correlations for minimised dimensionless thermal resistance and the dimensionless pressure difference for isosceles right and equilateral triangular channels. These correlations are obtained when the cooling geometry is optimised in order to achieve cooling for $\phi = 0.2$, where

$$R_{\min,\,\mathrm{Tri\,(I\text{-}T)}} = 7.62Be^{-0.49}, \qquad R^2 = 0.999 \tag{6.60}$$

$$R_{\min,\,\mathrm{Tri\,(E\text{-}T)}} = 7.66Be^{-0.49}, \qquad R^2 = 0.999 \tag{6.61}$$

where R^2 is the coefficient of correlation. The correlation given in Equations (6.60) and (6.61) correlate within the error of less than 0.01 to the CFD results produced.

6.3.9.2. Effect of applied dimensionless pressure difference on optimised design variables

Figure 6.35 shows the effect of the applied dimensionless pressure difference on the optimised dimensionless hydraulic diameter for the two triangular configurations. The curves show that the optimised dimensionless hydraulic diameter decreases as the applied dimensionless pressure difference increases for different porosities. This shows that unique optimal design geometry exists for each applied dimensionless pressure difference and porosity for all the configurations.

The numerical and approximate solutions at optimal geometry dimensions are in good agreement and the solutions follow similar trends as shown in Figures 6.35. However, the deviations are attributed to simplifying assumptions made in the formulation of the theoretical solution.

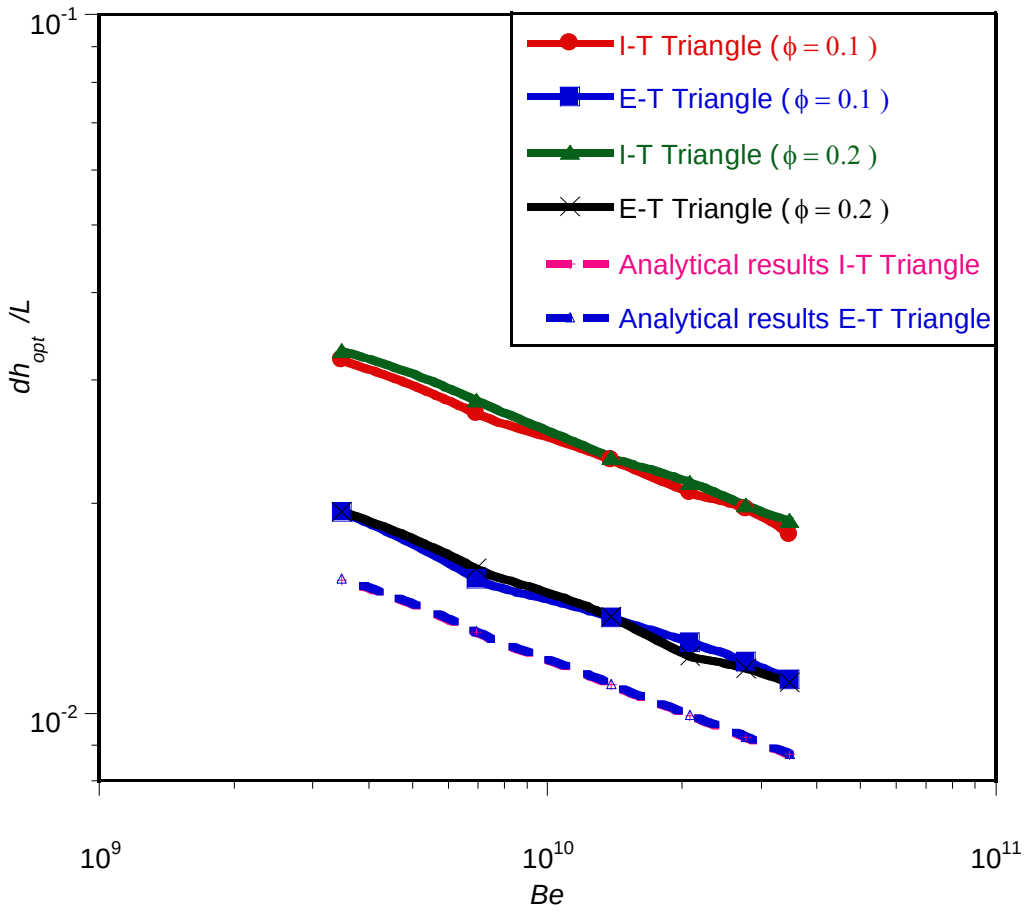

Figure 6. 35 : Correlation between the numerical and analytical solutions for the optimised hydraulic diameter

6.3.10. Optimal temperature contours

Figures 6.36(a) and 6.36(b) show the temperature contours of the elemental structure and the inner wall of the cooling channel with cooling fluid for equilateral triangular configurations, respectively. The blue region indicates the region of low temperature and the red region indicates that of high temperature. The arrow indicates the direction of flow.

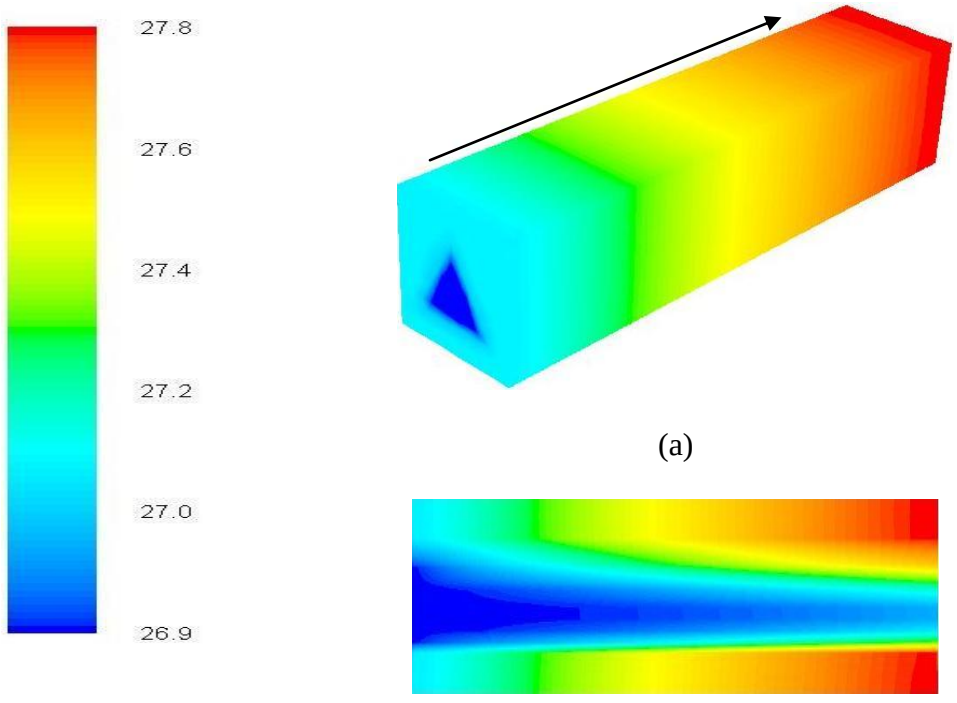

Figure 6. 36 : Temperature distributions on the cooling fluid and inner wall, as well as unit structure

6.4. CASE STUDY 3: RECTANGULAR COOLING CHANNEL EMBEDDED IN A HIGH-CONDUCTING SOLID

This present case study examines the three-dimensional numerical thermal resistance analysis in a heat-generated volume with rectangular cooling channels. The schematic physical configuration is shown in Figure 5.1(d). A computational elemental volume cell will also be modelled because of the symmetrical heat distribution as shown in Figure 6.37. The DYNAMIC-Q optimisation algorithm is used to search the optimal peak temperature (hence thermal resistance) by varying the geometric parameters subject to various constraints. The numerical optimisation results obtained will then be compared with it analytical solution in the preceding chapter.

6.4.1. Computational model

6.4.1.1. Design variables for isosceles rectangular cooling channels

In Figure 6.37, an elemental volume constraint is considered to be composed of an elemental cooling channel of width w_c , height h_c , and the surrounding solid of thickness $s_1$and s_2 which is defined as

$$v_{el} = whL \tag{6.62}$$

$$w = w_c + s_1 \tag{6.63}$$

$$h = h_c + s_2 \tag{6.64}$$

The volume of the elemental rectangular channel is:

$$v_c = w_c h_c L \tag{6.65}$$

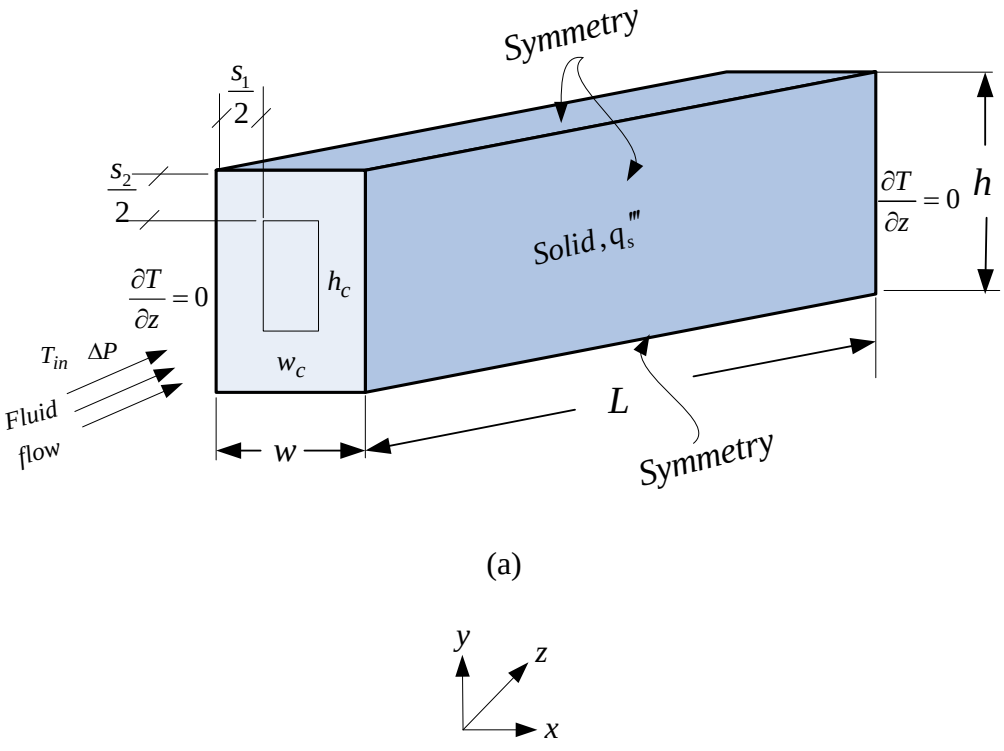

Figure 6. 37 : The boundary conditions of the three-dimensional computational domain of the cooling channel

Hence the number of channels in the structure arrangement can be defined as

$$N = \frac{HW}{hw} = \frac{HW}{(h_c + s_2)(w_c + s_1)} \tag{6.66}$$

However, porosity or void fraction of the unit structure is defined as

$$\phi = \frac{v_c}{v_{el}} = \frac{h_c w_c}{hw} \tag{6.67}$$

Aspect ratio of the unit structure is defined as

$$AR_s = \frac{h}{w} \tag{6.68}$$

Aspect ratio of the elemental channel is defined as

$$AR_c = \frac{h_c}{w_c} \tag{6.69}$$

The temperature distribution in the model was determined by solving the equation for the conservation of mass, momentum and energy numerically. The discretised three-dimensional computational domain of the rectangular configuration is shown in Figure 6.38. The cooling fluid was again water, as it is assumed to be in single-phase, steady, and a Newtonian fluid with constant thermo-physical properties. It was forced through the cooling channels by a specified pressure difference ΔP across the axial length of the structure.

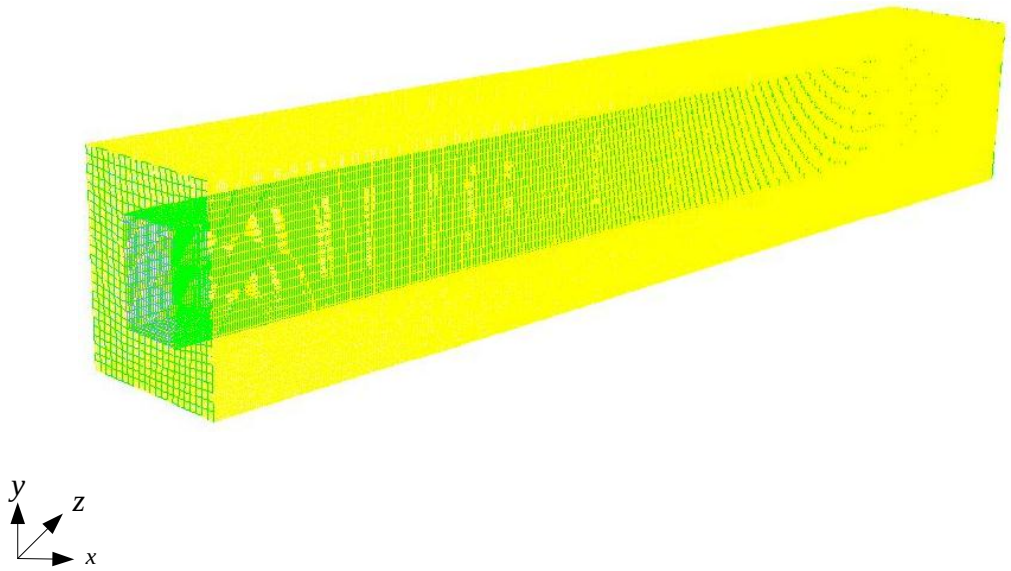

Figure 6. 38 : The discretised 3-D computational rectangualr cooling channels domain

Other assumptions imposed on the rectangular configuration model include, the solid structure top while the bottom right and left sides of the solid surfaces of the domain were taken as symmetry boundary conditions. All the outside walls were taken as plane of symmetry of the solid structure and were modelled as adiabatic as shown in Figure 6.37.

The objective function here is the minimum global thermal resistance as expressed in a dimensionless form in Equation (6.13)

and it is a function of the optimised design variables and the peak temperature,

$$R_{\min} = f\left(AR, d_h, s_1, s_2, \phi, \left(T_{\max}\right)_{\min}\right) \tag{6.70}$$

6.4.2. Numerical procedure

The procedure for numerical simulation used here is the similar (with little modification) to that of circular and square configurations discussed in Section 6.2.2. The simulation work began by fixing the length of the channel, applied pressure difference, porosity, internal heat generation, material properties and the elemental volume of the structure. We kept varying the values of the aspect ratio and the hydraulic diameter of the channel so as to identify the best (optimal) internal configuration that minimised the peak temperature.

The numerical solution of the of continuity, momentum and energy equations (Equations (3.1) to (3.8) of Chapter 3), along with the boundary conditions the two triangular configurations (Equations (6.58) to (6.66)), was obtained over the discretised domain shown in Figure 6.38. A three-dimensional finite volume commercial package FLUENT™ [199] was used, coupled with the geometry and mesh generation package GAMBIT [24] using MATLAB [219]. The GAMBIT [201] journal files for the rectangular configurations are supplied in Appendix B.5. The FLUENT [199] journal file in Appendix C is applicable to the simulations for which little modification is required in respect of the simulation boundary conditions.

6.4.3. Grid analysis and code validation

To ensure accurate results, several grid independence tests were conducted until a mesh size with negligible changes in peak temperature was obtained. Table 6.3 shows the grid independence test for a rectangular configuration for v_{el} = 1.8 mm^3 , w=150 μm, h = 1200 μm, $\emptyset$ = 0.2, AR_C = 8, a fixed length of L = 10 mm and fixed applied pressure differences of ΔP=50 kPa. Also, computational cell densities of 57 720, 101 250 and 125 100 were used for the grid independence test. It was observed that almost identical results were predicted when 101 250 and 125 100 cells were used. This implies that a further increase in the cell density beyond 101 250 had a negligible effect on the numerical result. The convergence criterion for the overall thermal resistance as the quantity monitored is given as in Equation (6.19).

Table 6. 3 : Grid independence study for rectangular configuration for w=150 μm, h = 1200 μm, ϕ = 0.2, AR_C = 8 and $\Delta P = 50\ kPa$

Number of nodes	Number of cells	T_{max}	$\gamma = \frac{\left\|(T_{max})_i - (T_{max})_{i-1}\right\|}{\left\|(T_{max})_i\right\|}$
45 379	30 000	27.65323	-
81 938	57 720	27.65759	0.000158
136 780	101 250	27.71466	0.002059
168 362	125 100	27.71188	0.0001

6.4.4. Numerical results

In this section, we attempt to show that there was an optimal geometry that minimised the peak temperature. The results were presented for the case where vel = 1.8 $mm^{3,}$

w=150 μm, $\varnothing$ = 0.2, h = 1200 μm, a fixed length of L = 10 mm and fixed applied pressure differences of ΔP=50 kPa.

Figures 6.39 and 6.40 show the existence of an optimum aspect ratio and optimum hydraulic diameter of the cooling channel in which the peak temperature is minimised at any point in the channel. Figures 6.39 shows that peak temperature strongly depends on aspect ratio. The peak temperature decreases as the aspect ratio increases. However, at very higher AR, the peak temperature increases. Figure 6.40 is the graph that shows peak temperature as a function of the channel hydraulic diameter. It shows the existence of an optimum hydraulic diameter of the cooling channel where the peak temperature is minimised at any point in the channel. The channel hydraulic diameter has a significant effect on the peak temperature and the overall thermal resistance. It shows that there exists an optimal channel hydraulic diameter that lies in the range $0.005 \leq d_h /L \leq 0.015$ and that minimises the peak temperature. Hence, peak temperature decreases as d_h /L decreases and a minimum value is reached beyond which the peak temperature begins to increase.

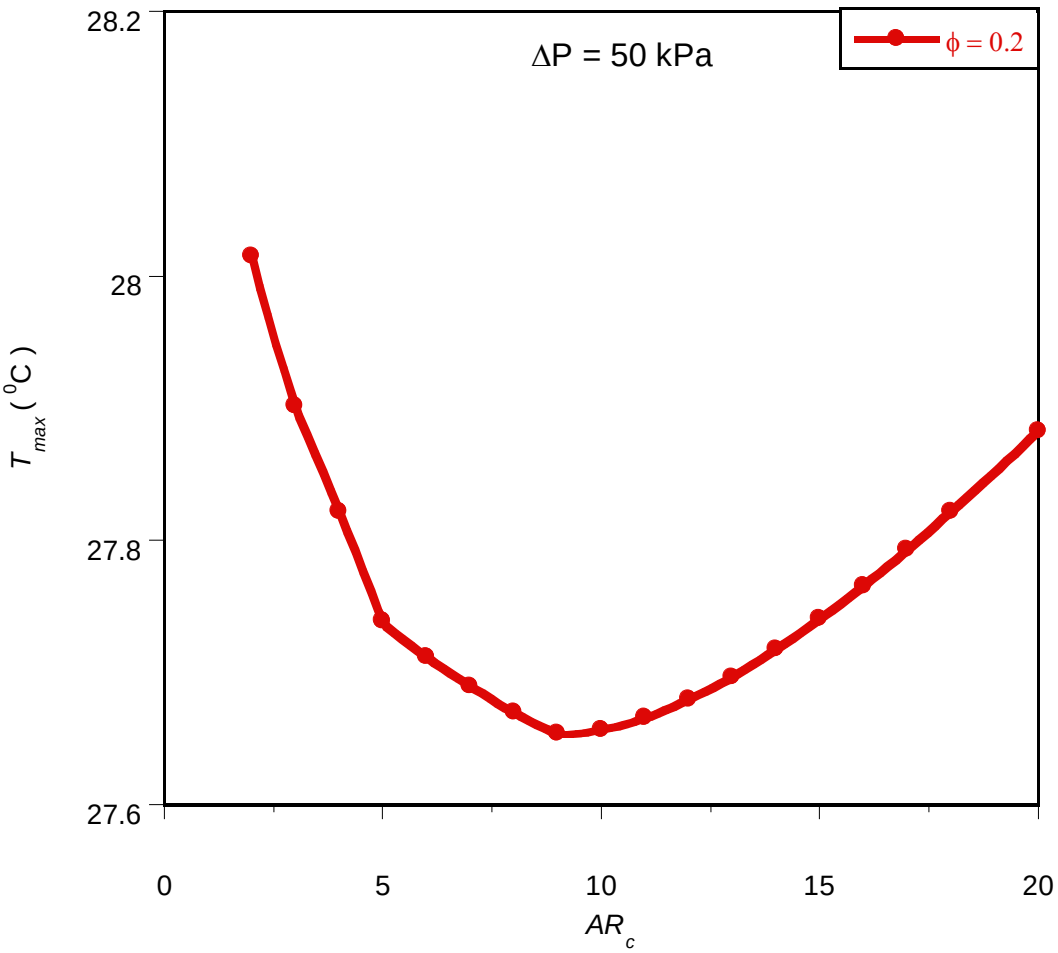

Figure 6. 39 : Effect of the optimised dimensionless channel aspect ratio AR_c on the peak temperature

Therefore, the global thermal resistance decreases as the hydraulic diameter increases. Also, the global thermal resistance decreases as the hydraulic diameter decreases. Any hydraulic diameter values above or below the optimal ranges, will cause the working fluid to be not properly engaged in the cooling process. This process is detrimental to the global performance of the system.

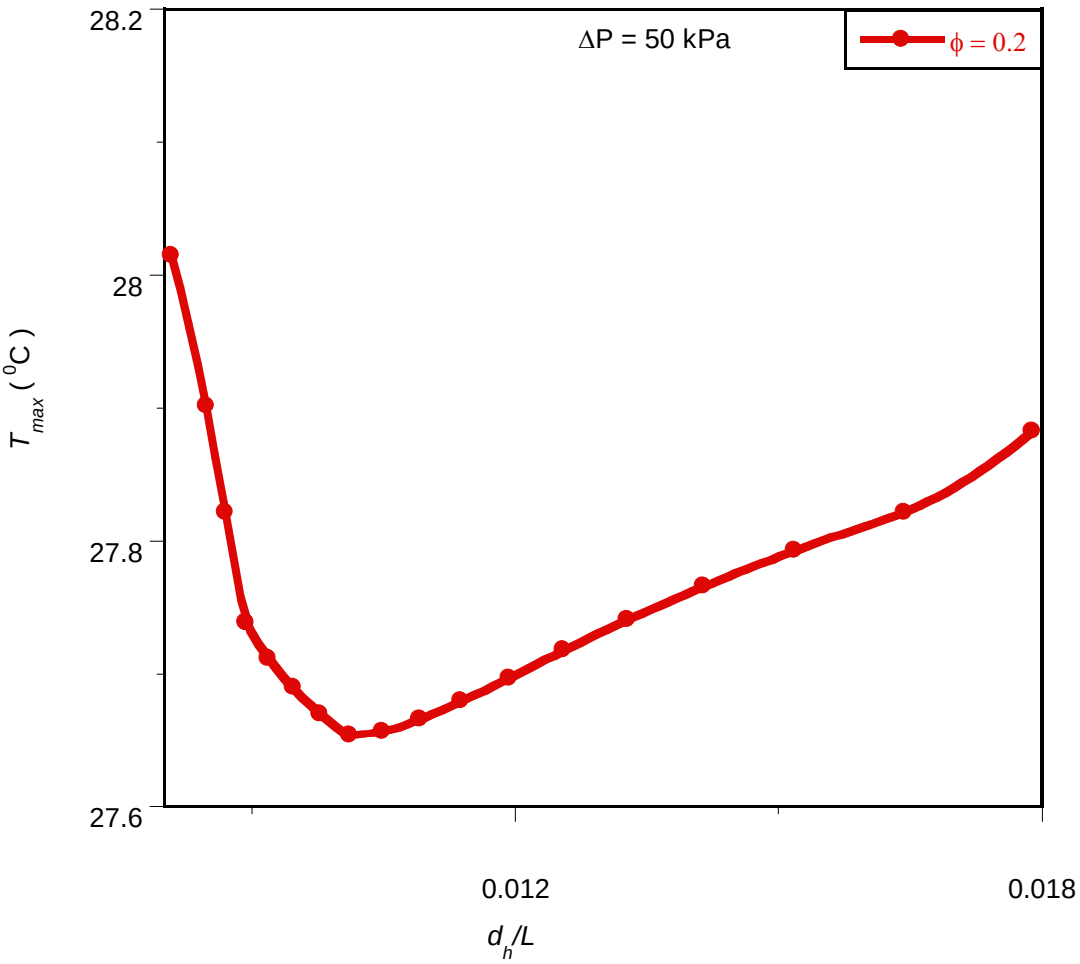

Figure 6. 40 : Effect of the optimised hydraulic diameter d_h , on the peak temperature

6.4.5. Mathematical formulation of the optimisation problem

We again introduce a mathematical optimisation algorithm that will search and identify the optimal design variables at which the system will perform at an optimum. the objective function is the minimisation of global thermal resistance.

6.4.5.1. Optimisation problem and design variable constraints

The optimisation technique described in Section 6.2.5 was applied to the rectangular model described in section 6.4.1.

The constraint ranges for the rectangular configuration optimisation are as follows:

$$0.1 \leq \phi \leq 0.2 \tag{6.71}$$

$$1 \leq AR_s \leq 20 \tag{6.72}$$

$$1 \leq AR_c \leq 20 \tag{6.73}$$

$$v_{el} = 1.8\ mm^3 \tag{6.74}$$

$$0 \leq w \leq L \tag{6.75}$$

$$0 \leq w_c \leq w \tag{6.76}$$

$$0 \leq h_c \leq h \tag{6.77}$$

$$0 \leq s_1 \leq w \tag{6.78}$$

$$0 \leq s_2 \leq h \tag{6.79}$$

The optimisation process was repeated for pressure differences across the axial length, ranging from 5 *kPa* to 50 *kPa* within the design constraint ranges given in Equations (6.71) to (6.79). This is done in order to search for and identify of the channel layout that minimises the peak temperature, T_{max} so that the minimum thermal resistance

between the fixed volume and the cooling fluid is obtained as the desired objectives function.

6.4.6. Mathematical statement of the optimisation problem

The variables chosen for the mathematical statement are:

$$x_1 = w \tag{6.80}$$

$$x_2 = h \tag{6.81}$$

$$x_3 = w_c \tag{6.82}$$

$$x_4 = h_c \tag{6.83}$$

Substituting Equations (6.80) to (6.83) for Equations (6.71) to (6.79), results in the objective and constraints functions given in Equations (6.84) to (6.92). The inequality functions g_1(x) and g_2(x) are derived from the porosity constraint of Equation (6.67).

The mathematical statement of the optimisation problem for rectangular configuration can then be written as:

$$f(x) = T_{\max} \tag{6.84}$$

$$g_1(x) = 0.0018 - x_3 x_4 \leq 0 \tag{6.85}$$

$$g_2(x) = 0.0036 - x_3 x_4 \leq 0 \tag{6.86}$$

$$g_3(x) = -x_1 - x_2 \leq 0 \tag{6.87}$$

$$g_4(x) = -x_2 - 20x_1 \leq 0 \tag{6.88}$$

$$g_5(x) = -x_3 - x_4 \leq 0 \tag{6.89}$$

$$g_6(x) = -x_4 - 20x_3 \leq 0 \tag{6.90}$$

$$g_7(x) = -x_3 - x_1 \leq 0 \tag{6.91}$$

$$g_8(x) = -x_4 - x_2 \leq 0 \tag{6.92}$$

6.4.7. Sensitivity analysis of selecting the forward differencing step size

Figure 6.41 shows the graph of peak temperature as a function of the height of rectangular cooling channels with a similar sensitivity analysis procedure for cylindrical cooling channel with step sizes of 10^{-6} and 10^{-4}. Although, different values of the step size of height of rectangular cooling channel as design variable were considered such as 10^{-6}, 10^{-5}, 10^{-4} and 10^{-3}. A Figures 6.42 shows graph of peak temperature as a function of channel width, with a candidate step size of 10^{-4}.

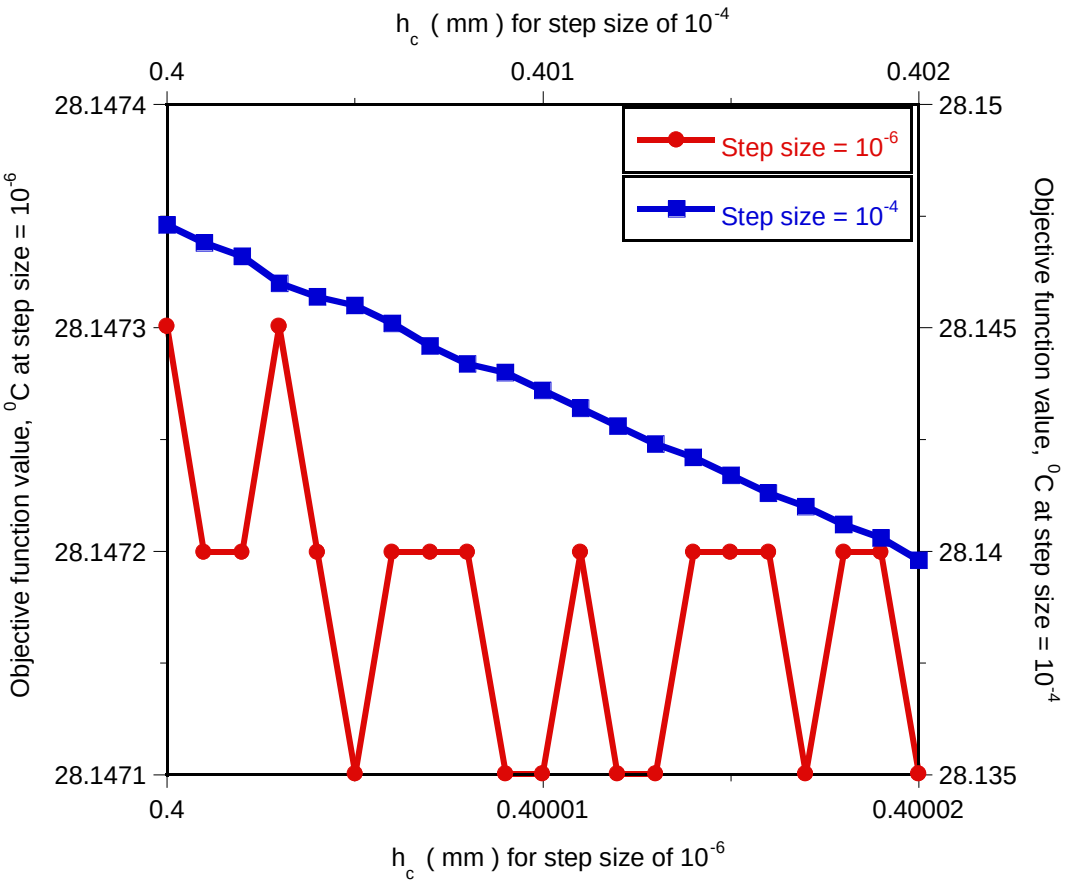

Figure 6. 41 : Plotting temperature for different channel height values with step sizes of 10^{-6} and 10^{-4}

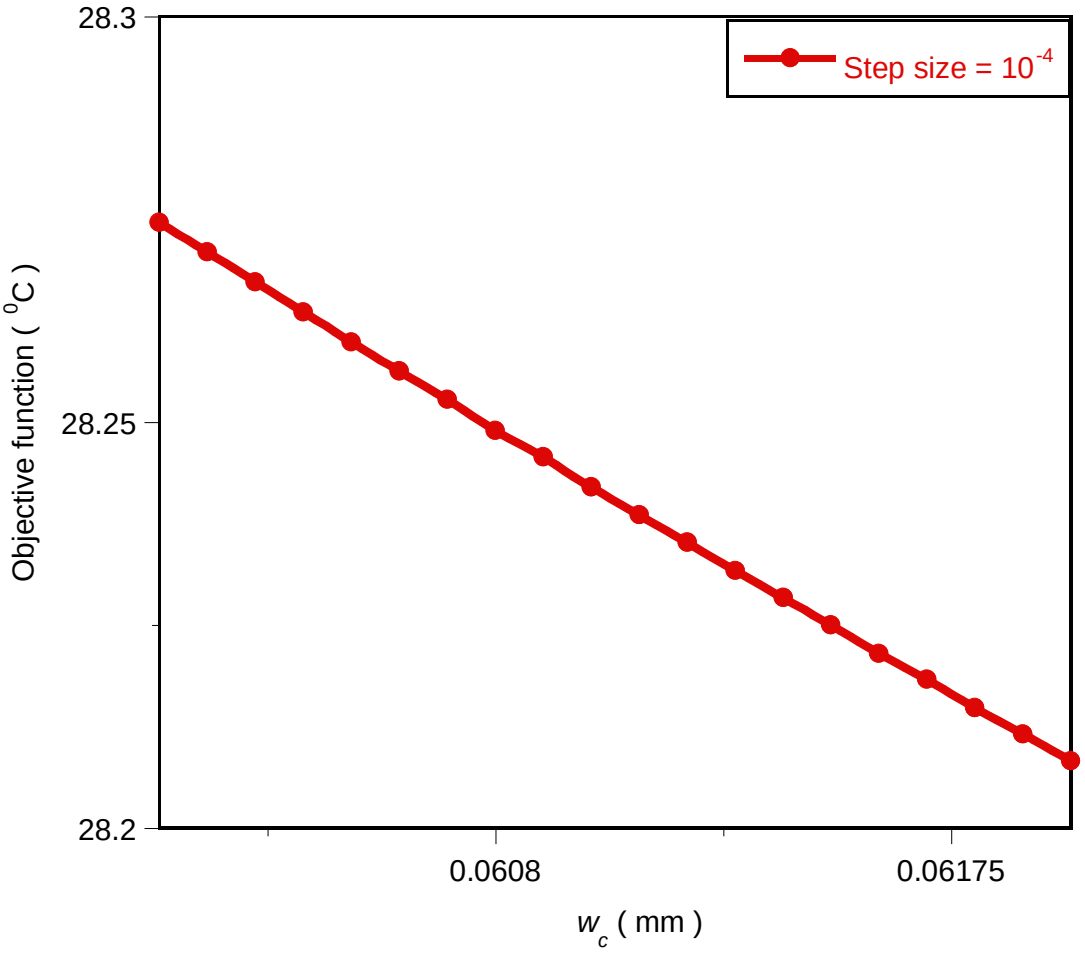

Figure 6. 42: Plotting temperature for different channels width values with a step size of 10^{-4}

6.4.8. Optimisation results

6.4.8.1. Effect of applied pressure difference on optimised geometry and minimised thermal resistance

Figure 6.43 shows the minimised dimensionless global thermal resistance as a function of dimensionless pressure difference at optimised design variables for the configuration. The results show that the dimensionless minimised global thermal resistance decreases as the dimensionless pressure difference increases. This trend is in agreement with previous work [94].

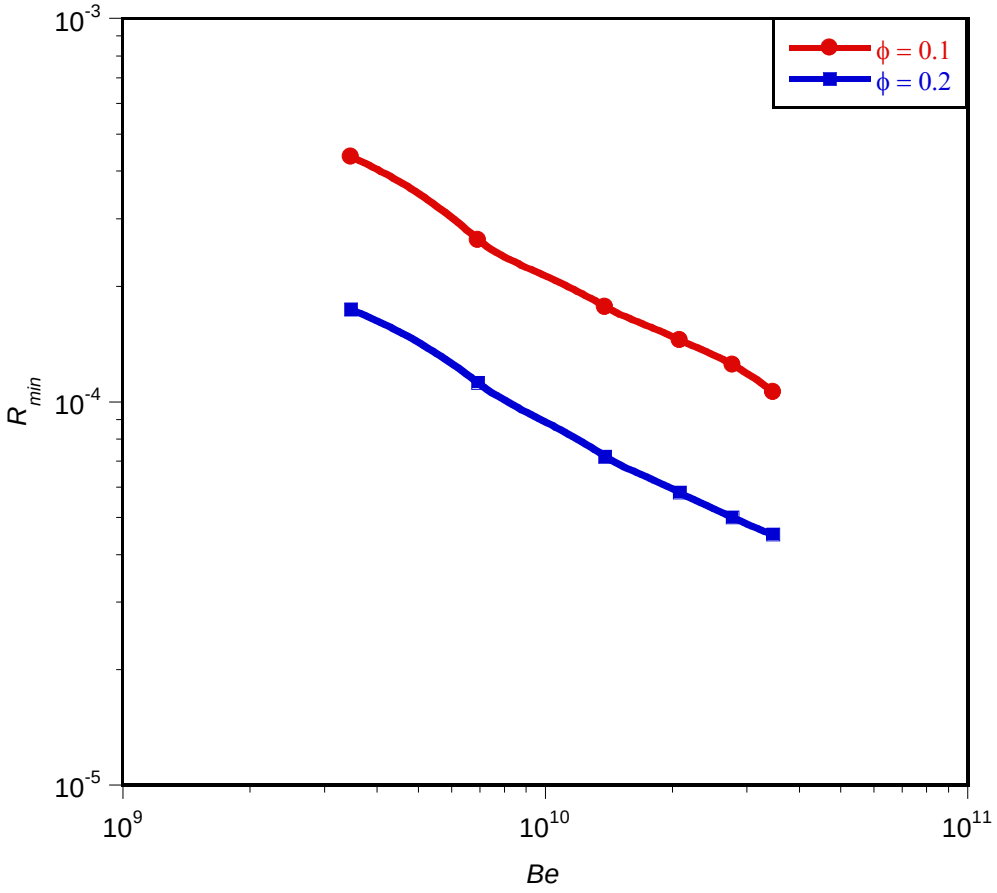

Figure 6. 43 : Effect of dimensionless pressure difference on the minimised dimensionless global thermal resistance

Figures 6.44 to 6.46 show the optimal behaviours of the geometry with respect to applied pressure difference (or Bejan number). It is shown that unique optimal design

geometries exist for each applied dimensionless pressure difference. Figure 6.44 shows that the optimised channel aspect ratio increases as the applied dimensionless pressure difference and porosity increase. Also, in Figures 6.43 and 6.45, it is clearly observed that the global dimensionless thermal resistance decreases as the channel aspect ratio increase. However, it is recognised that the optimal design scheme could lead to a design that could be impractical at very high channel aspect ratios, due to the channel being too thin to be manufactured.

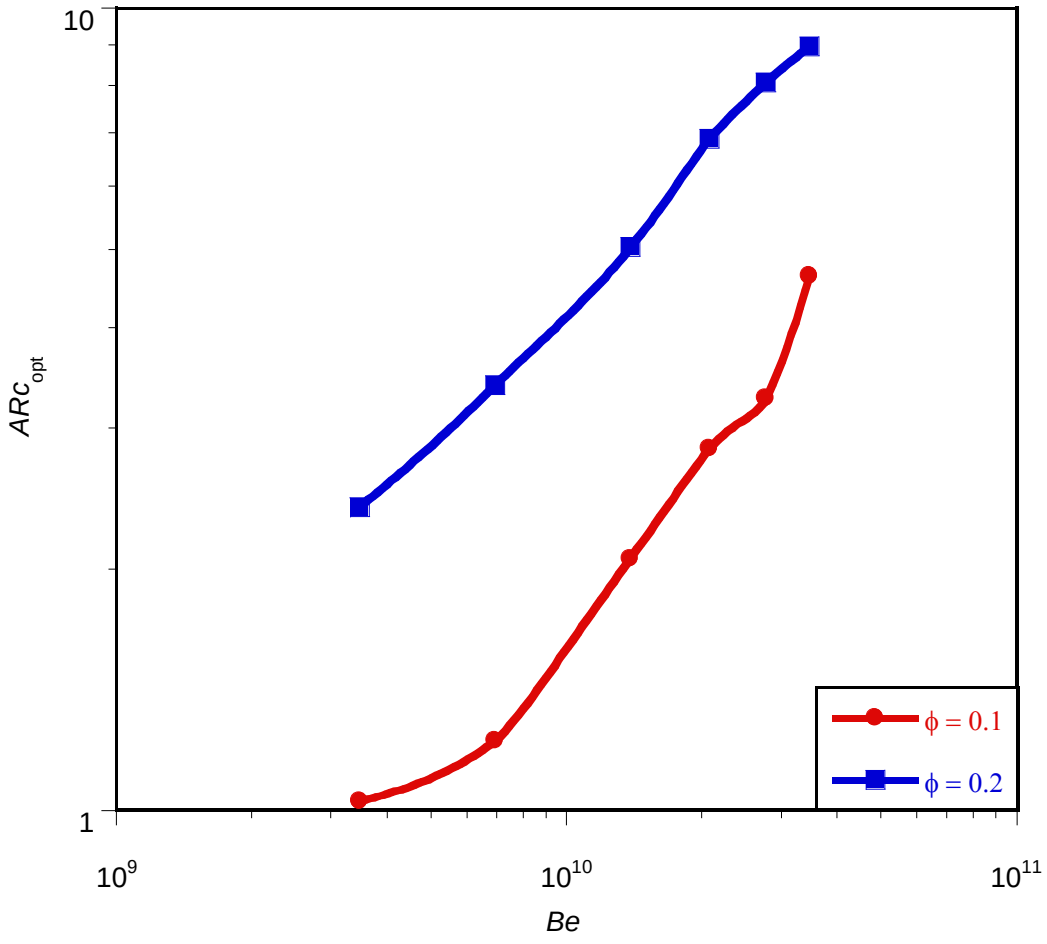

Figure 6. 44 : Effects of dimensionless pressure difference on the optimised aspect ratio

Figures 6.45 and 6.46 show the effect of the dimensionless pressure difference on the optimised dimensionless design variable. Figure 6.45 shows that the optimal hydraulic diameter decreases as the pressure differences increase. Also, Figure 6.46 shows that the optimal channels spacing $(s_1/s_2)_{opt}$ increases as the dimensionless pressure difference increases. We can say that there exists a unique optimal geometry for each of the applied pressure differences. The trend is in agreement with previous work. The trends of these results are also in agreement with previous work [94].

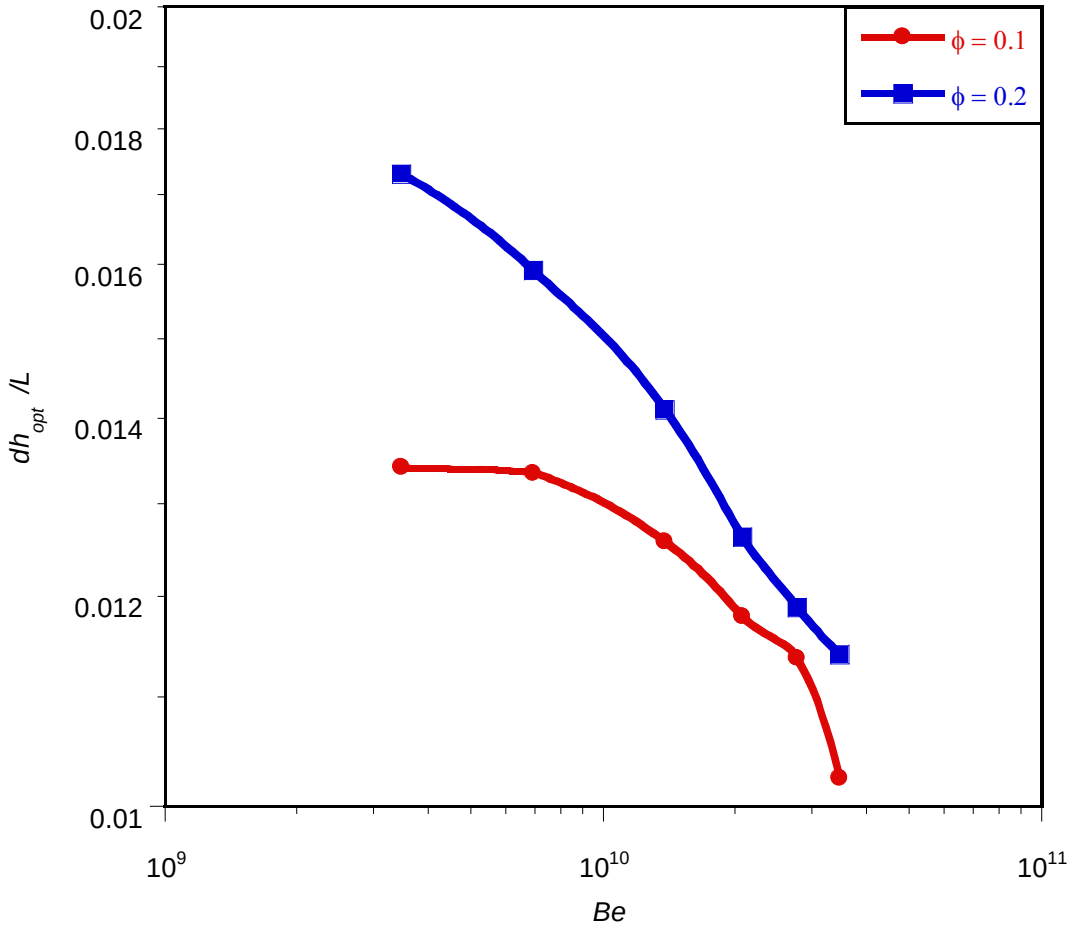

Figure 6. 45 : Effect of dimensionless pressure difference on the optimised hydraulic diameter

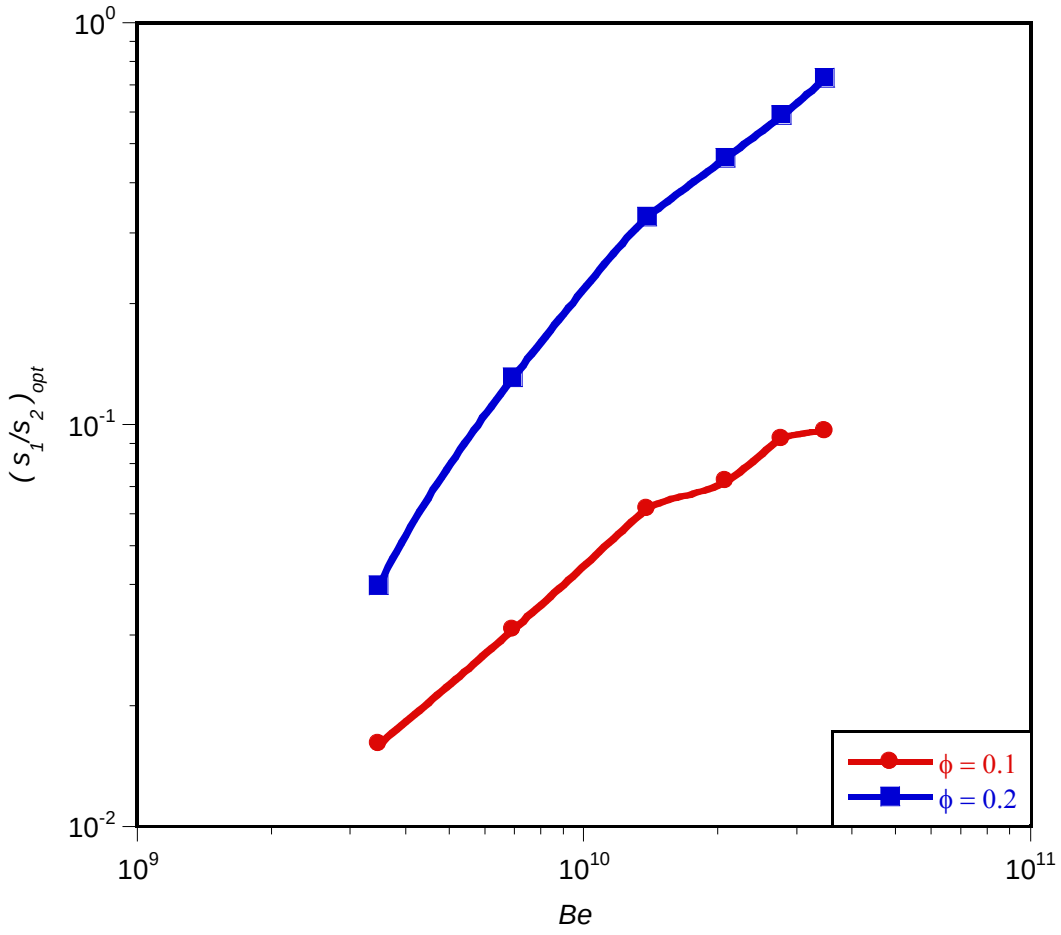

Figure 6. 46 : Effect of dimensionless pressure difference on the optimised channel spacing ratio

6.4.9. Comparison of the theoretical method and numerical optimisation

6.4.9.1. Effect of the applied dimensionless pressure difference on the minimised dimensionless global thermal resistance

The analytical results of Equation (5.39) were used to validate the numerical solutions. The numerical and approximate solutions, based on scale analysis at

optimal geometry dimensions, are in good agreement and the solutions follow similar trends as shown in Figure 6.47. Although the analytical results are lower than the numerical results, the theoretical and numerical values agree within a factor of 1.5 for the worst case. However, these deviations are attributed to simplifying assumptions made in the formulation of the theoretical solution. These results are also in agreement with past research work [94].

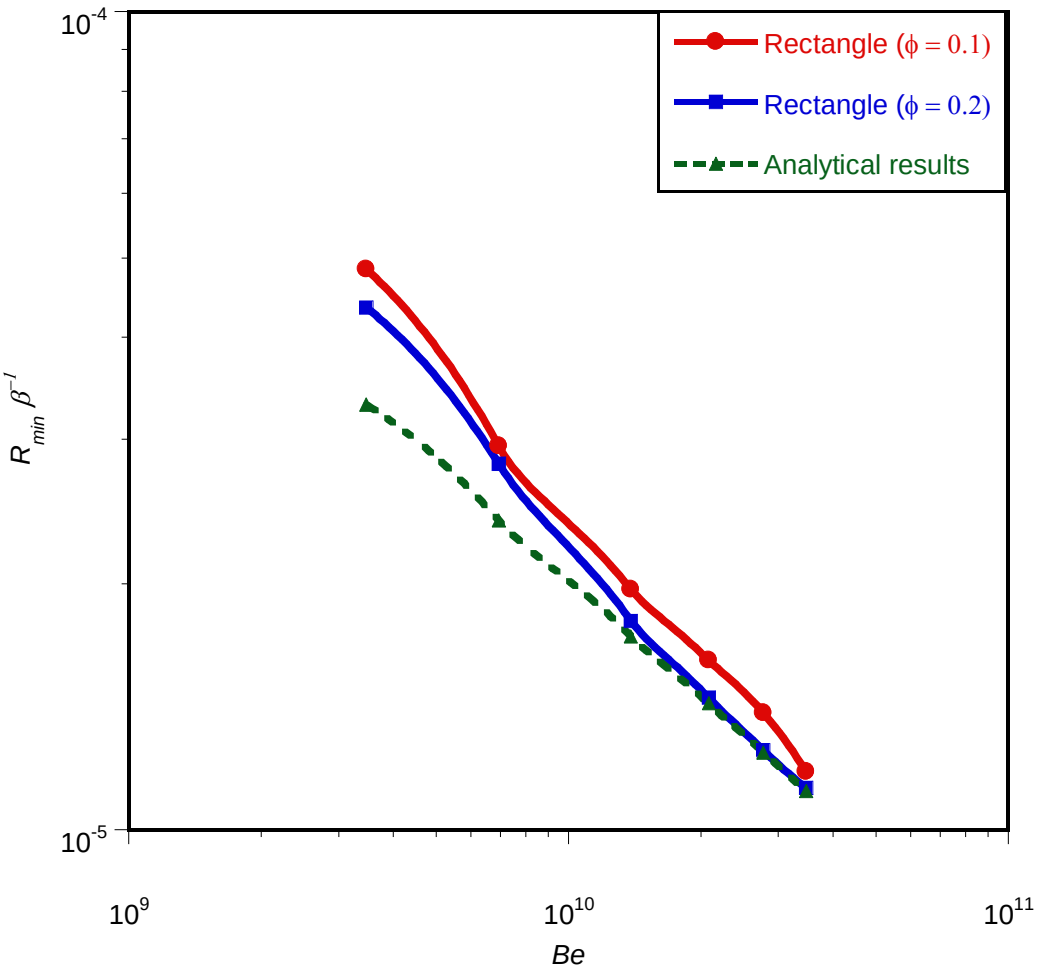

Figure 6. 47 : Correlation of the numerical and analytical solutions for the minimised global thermal resistance

Equation (6.93) presents the correlations for minimised dimensionless thermal resistance and the dimensionless pressure difference that is obtained when the cooling geometry is optimised to achieve cooling.

$$R_{\min} = \alpha B e^{-\beta} \tag{6.93}$$

where α and β are constant that depend on porosity and scale effects. For porosity of 0.2, α and β are 62.07 and 0.59 respectively within the error of less than 0.01.

6.4.9.2. Effect of dimensionless pressure difference on optimised design variables

Figure 6.48 shows the effect of the dimensionless pressure difference on the optimised dimensionless hydraulic diameter for the two triangular configurations. The curves show that the optimised dimensionless hydraulic diameter decreases as the applied dimensionless pressure difference increases for different porosities. This shows that, for all the configurations, unique optimal design geometry exists for each applied dimensionless pressure difference and porosity .

The numerical and approximate solutions at optimal geometry dimensions are in good agreement and the solutions follow similar trends as shown in Figures 6.48. However, the deviations are attributed to simplifying assumptions made in the formulation of the theoretical solution.

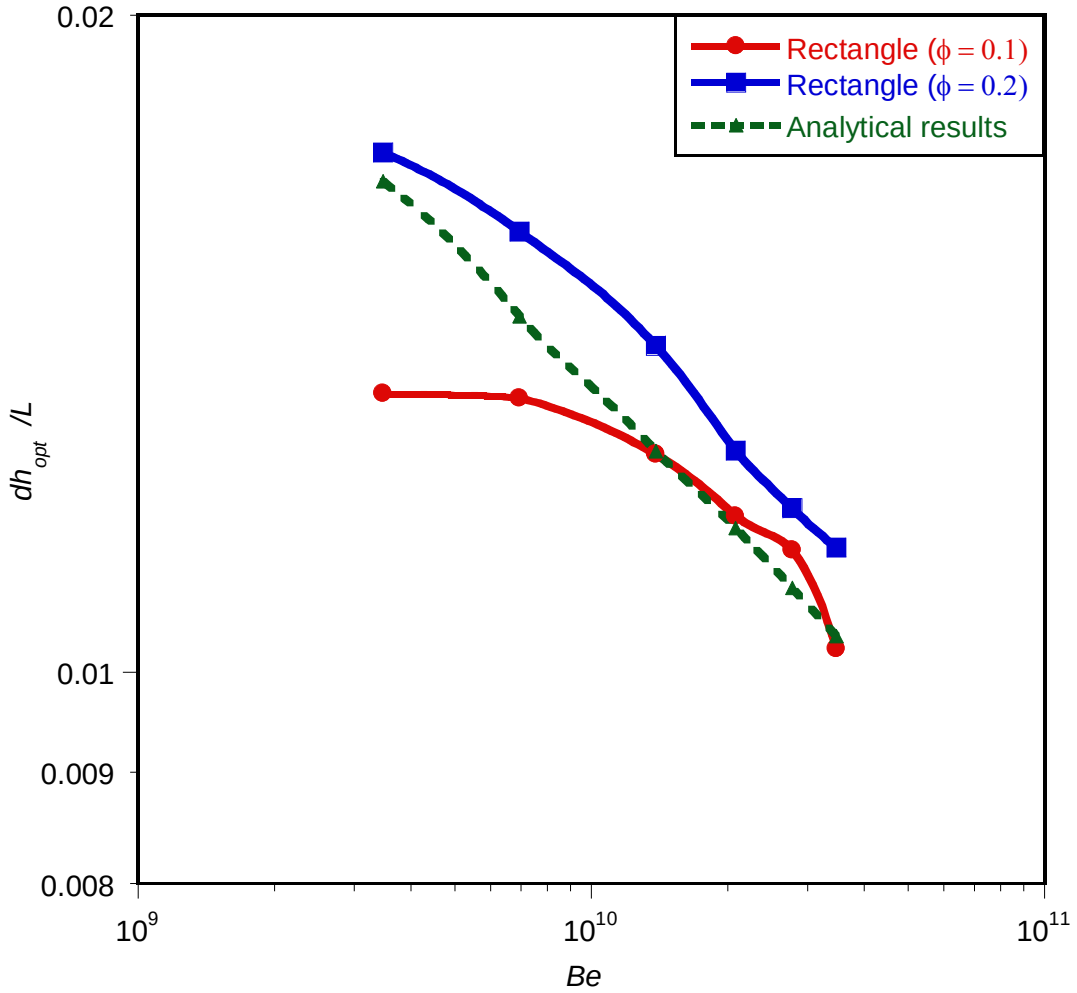

Figure 6. 48 : Correlation of numerical and analytical solutions for the optimised hydraulic diameter

6.4.9.3. Optimisation problem and design variable constraints

Figures 6.49(a) and 6.49(b) shows the temperature contours of the elemental structure and the inner wall of the cooling channel with cooling fluid for rectangular configuration respectively. The blue region indicates the region of low temperature

and the red region indicates that of high temperature. The arrow indicates the direction of flow.

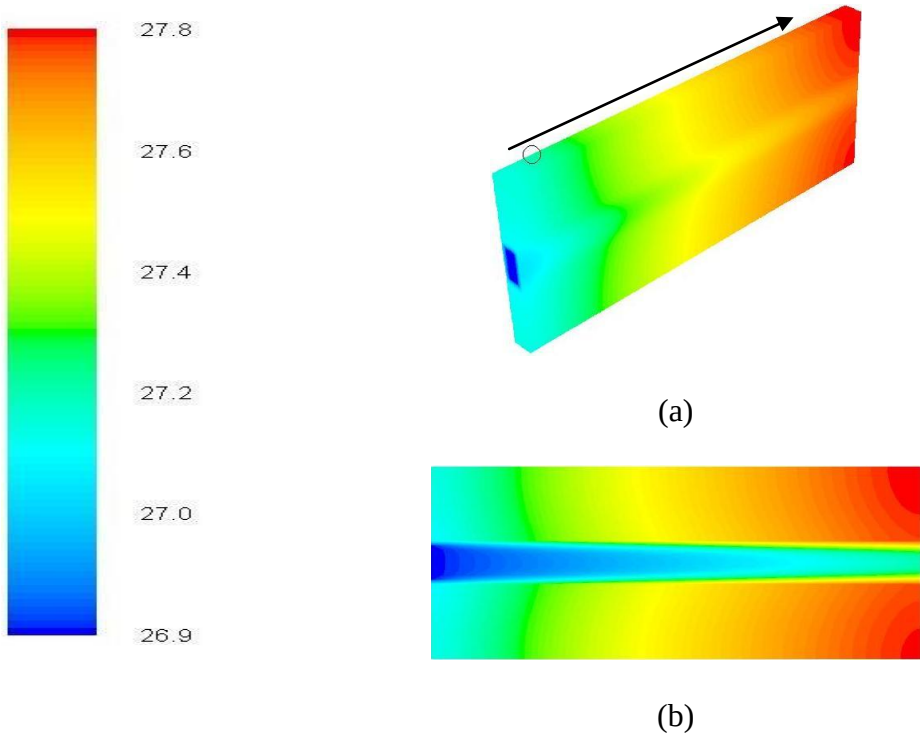

Figure 6. 49 : Temperature distribution on (a) the unit structure and (b) the cooling fluid and inner wall

6.4.10. Comparison and Summarised trends of all the case studies

In the preceding sections, the thermal performances of cooling channels with different cross-sectional shapes were determined by numerically optimising their geometrical parameters. The shapes of the cooling channels studied were, circular, square, isosceles right triangular, equilateral triangular and rectangular. In this section, we summarise trends by comparing all the optimisation cases studied.

Figure 6.50 shows the minimised thermal resistance of all the cooling channels studied as a function of applied dimensionless pressure difference number under uniform heat-generation thermal boundary conditions. As shown in Figure 6.48, all cases of channel shapes studied show a similar increasing trend in their thermal performances with an increase in dimensionless pressure difference number. The optimised numerical solutions show a linear decrease in the minimised global thermal resistance with increasing applied dimensionless pressure difference number.

From these results, it was also observed that the thermal performance of the cylindrical channel was poorer than that of any of the other four configurations.

The isosceles triangular configuration gave the best thermal performance followed by the equilateral triangular configuration. Next in the rank was the rectangular shape and followed by the square channel. This is due to the fact that triangular configurations have high shear stress corners. These findings are all in agreement with analytical solutions provided in Chapter 5.

However, it was clearly observed that the cooling effect was best achieved at a higher aspect ratio of rectangular channels. The optimal design scheme could well lead to a design that would be impractical at very high channel aspect ratios, due to the channel being too thin to be manufactured. Details of the results can be seen in Table 6.4 and 6.5.

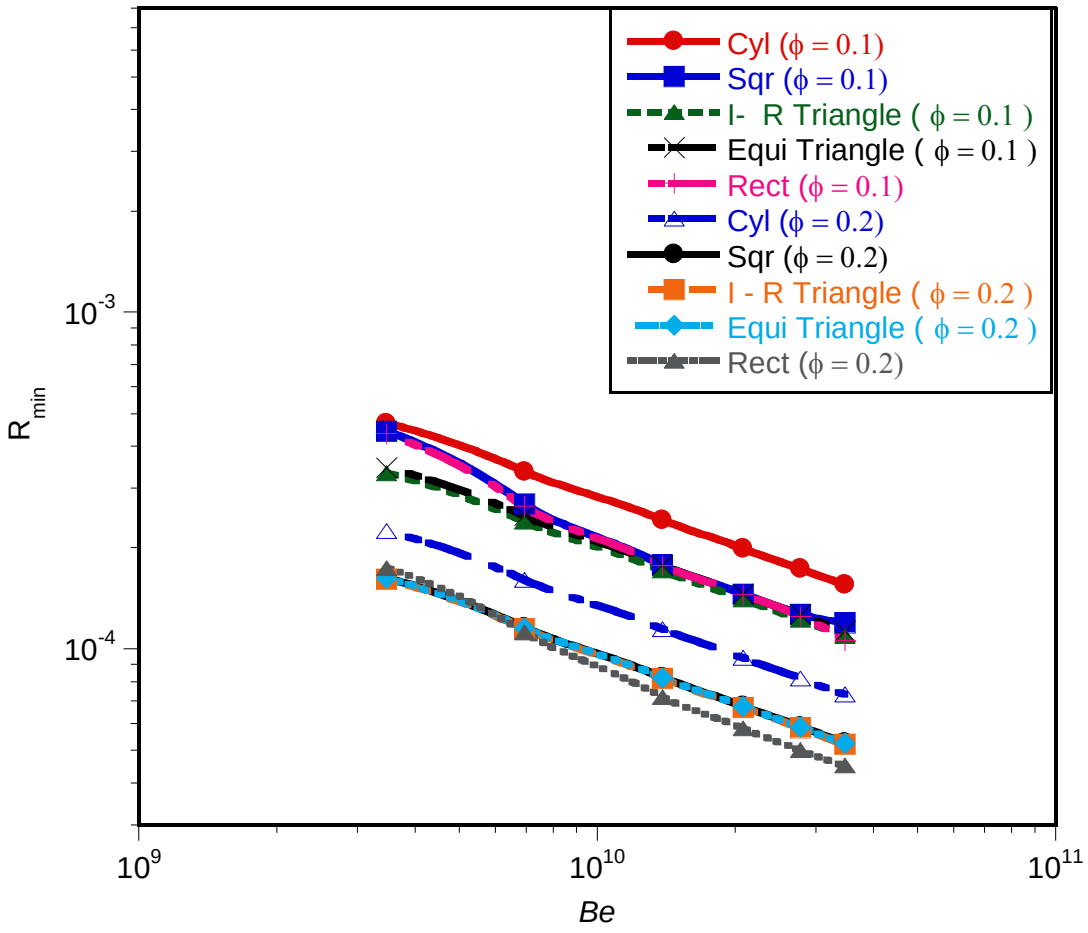

Figure 6. 50 : Comparison of the thermal performance of the cooling channels shapes studied

Table 2: Minimised global thermal resistance, R_{min} at $\phi = 0.1$ for all the cases shapes studied

	R_{min}	R_{min}	R_{min}	R_{min}	R_{min}
	Cylinder	Square	Isosceles	Equilateral	Rectangle
3.47E+09	0.0004685	0.0003333	0.0003327	0.0003449	0.00043600
6.94E+09	0.0003365	0.0002391	0.0002387	0.0002484	0.00026500
1.39E+10	0.0002414	0.0001712	0.0001709	0.0001771	0.00017700
2.08E+10	0.0001986	0.0001406	0.0001403	0.0001453	0.00014500
2.77E+10	0.0001728	0.0001228	0.0001220	0.0001262	0.00012500
3.47E+10	0.0001552	0.0001097	0.0001093	0.0001130	0.00010600

Table 1: Minimised global thermal resistance, R_{min} at $\phi = 0.2$ for all the cases shapes studied

Be	R_{min}	R_{min}	R_{min}	R_{min}	R_{min}
	Cylinder	Square	Isosceles	Equilateral	Rectangle
3.47E+09	0.0002241	0.0001624	0.0001611	0.0001620	0.00017400
6.94E+09	0.0001603	0.0001156	0.0001147	0.0001153	0.00011200
1.39E+10	0.0001146	0.0000823	0.0000816	0.0000821	7.2000e-05
2.08E+10	0.0000940	0.0000675	0.0000670	0.0000674	5.8000e-05
2.77E+10	0.0000817	0.0000587	0.0000582	0.0000585	5.0000e-05
3.47E+10	0.0000732	0.0000526	0.0000521	0.0000524	4.5000e-05

6.5. CONCLUSION

This chapter demonstrates a numerical optimisation methodology of conjugate heat transfer in cooling channels of different cross-sectional shapes with the help of a multidimensional and robust gradient-based optimisation algorithm. Global optimal solutions are obtained using Dynamic-Q, which does not require an explicit line search.

The shapes of the cooling channels studied were, circular, square, isosceles right triangular, equilateral triangular and rectangular. These cooling channels of different shapes penetrated and embedded in a highly conductive solid material were optimised. The overall objective of all these cases was to minimise the peak wall temperature of the conductive solid structure in order to achieve lowered thermal resistances. Under a fixed volume and other material constraints, relationships were developed between various optimal geometric parameters and the dimensionless pressure difference.

The temperature distribution of the different cooling channels shapes was analysed. Sensitivity analysis was performed to make sure CFD noise did not affect the optimal solutions. This highlights the importance of correct formulation and design set-up for effective and accurate optimisations.

It can be concluded that for all the geometrical shapes studied, the design variables had significant effect on the thermal performance of heat-generating devices. The optimisation reveals that there exist a trade-off between the global thermal resistance and the applied dimensionless pressure difference number (pumping power) in order to optimise the heat-generating devices and the channel configurations. The optimum design variables are sensitive to the applied dimensionless pressure difference number (*Be*) within the design space and show an alternating behaviour with change of the applied dimensionless pressure difference number. This shows the existence of unique optimal design variables (geometries) for a given applied dimensionless pressure number for each configuration studied. Therefore, thermal designers can pick an optimal solution according to the applied dimensionless pressure difference number (*Be*) available to drive the fluid or thermal resistance required.

The various case designs emphasised the fact that for cooling channels design, material cost and applied pressure difference considerations are vital elements in achieving optimal designs.

It is also observed that although the thermal performance of the cylindrical channel was poorer than that of any other channels, it was a more viable option and more often used in industry due to the ease of manufacturability and packaging.

The numerical results obtained are in good agreement with results obtained in the approximate solutions based on scale analysis at optimal geometry dimensions in Chapter 5. The approximate dimensionless global thermal resistance predicts the trend obtained in the numerical results. The use of the optimisation algorithm coupled to the CFD package render the numerical results more robust with respect to the selection of optimal structures' internal configurations of the flow channels and dimensionless pressure difference.